AFRL-AFOSR-VA-TR-2020-0036

A Multiscale Morphing Continuum Analysis on Energy Cascade of Compressible Turbulence

Mingjun Wei
KANSAS STATE UNIVERSITY

05/13/2020
Final Report

Air Force Research Laboratory
AF Office Of Scientific Research (AFOSR)/ RTA1
Arlington, Virginia 22203
Air Force Materiel Command

REPORT DOCUMENTATION PAGE

Form Approved
OMB No. 0704-0188

1. REPORT DATE *(DD-MM-YYYY)*	2. REPORT TYPE	3. DATES COVERED *(From - To)*
29-06-2020	Final Performance	15 Feb 2017 to 14 Feb 2020

4. TITLE AND SUBTITLE
A Multiscale Morphing Continuum Analysis on Energy Cascade of Compressible Turbulence

5a. CONTRACT NUMBER

5b. GRANT NUMBER
FA9550-17-1-0154

5c. PROGRAM ELEMENT NUMBER
61102F

6. AUTHOR(S)
Mingjun Wei, James Chen

5d. PROJECT NUMBER

5e. TASK NUMBER

5f. WORK UNIT NUMBER

7. PERFORMING ORGANIZATION NAME(S) AND ADDRESS(ES)
KANSAS STATE UNIVERSITY
2 FAIRCHILD HALL
MANHATTAN, KS 665061100 US

8. PERFORMING ORGANIZATION REPORT NUMBER

9. SPONSORING/MONITORING AGENCY NAME(S) AND ADDRESS(ES)
AF Office of Scientific Research
875 N. Randolph St. Room 3112
Arlington, VA 22203

10. SPONSOR/MONITOR'S ACRONYM(S)
AFRL/AFOSR RTA1

11. SPONSOR/MONITOR'S REPORT NUMBER(S)
AFRL-AFOSR-VA-TR-2020-0036

12. DISTRIBUTION/AVAILABILITY STATEMENT
A DISTRIBUTION UNLIMITED: PB Public Release

13. SUPPLEMENTARY NOTES

14. ABSTRACT
This project presents the kinetic nature of the morping continuum theory and its application in compressible turbulence and nonequilibrium phenomena at high Mach number. Numerious publications have indicated that morphing continuum theory is capable of predicting high speed and compressible turbulence physics without requiring heavy computational resources - saving about an order lower than the classical N.S.-based DNS for grids. The 2D and 3D test cases includes incompressible turbulence of Re~1M, supersonic turbulence of Mach 3 and transonic turbuelnce with weak shock. Morphing continuum theory can successfully capture the shock structure and heat transfer at high Mach number (Ma~10)

15. SUBJECT TERMS
Multiscale Morphing Continuum, compressible turbulence, energy cascade for compressible turbulence

16. SECURITY CLASSIFICATION OF:			17. LIMITATION OF ABSTRACT	18. NUMBER OF PAGES	19a. NAME OF RESPONSIBLE PERSON
a. REPORT	b. ABSTRACT	c. THIS PAGE			LEYVA, IVETT
Unclassified	Unclassified	Unclassified	UU		19b. TELEPHONE NUMBER *(Include area code)* 703-696-8478

Standard Form 298 (Rev. 8/98)
Prescribed by ANSI Std. Z39.18

(YIP) A Multiscale Morphing Continuum Analysis on Energy Cascade of Compressible Turbulence

PI: James Chen *
Final Report

Multiscale Computational Physics Lab
Department of Mechanical and Aerospace Engineering
University at Buffalo – The State University of New York

1 Goal and Major Achievements

The goal of the project is to construct a statistical morphing continuum theory to model the complex and non-equilibrium eddies in compressible turbulence. In the past three year, the team has (1) established the statistical basis of the morphing continuum theory; (2) validated a computationally effective numerical scheme for compressible turbulent flows; (3) investigated the application of morphing continuum theory for compressible turbulence, nonequilibrium flows and turbulence energy transfer. In Summer 2018, the PI and his research team also moved from Kansas State University (K-State) to University at Buffalo – The State University of New York (UB) to resume his academic career. In early 202, the PI was promoted to Associate Professor with tenure at UB. In the duration of the project, the team, including the PI and the graduate students, are recognized in numerous national and international awards.

Overall, the PI and his research team have published at least nine journals, five conference papers, eleven conference presentations and seven invited talks. Detailed publication list can be find in the later sections. There are four graduate students (one US citizen and three international students) supported in this project. This project also resulted in two students completing PhD degrees (in 2018 and 2020) and one receiving MS degree in 2020. The research outcome from this project has also been featured in more than 20 media outlets, including a feature article in Aerospace Testing International (a UK-based aerospace magazine) [64].

2 Kinetic Description of Morphing Continuum

A continuum theory can be deduced from a kinetics-based approach, e.g. Kinetic Theory, or a mathematics-based framework, e.g. rational continuum mechanics.

*funded by AFOSR through award number FA9550-17-1-0154

The team has established the kinetic foundation for morphing continuum at the equilibrium state [14, 15] previously. In the second year, the team further the derivation to a linear deviation from the equilibrium distribution to account for the nonequilibrium state of the fluid flows. Such derivations were also consistent with the governing equations deduced from rational continuum mechanics by Eringen [26] and Hansen [36]. The team also found the pathway to reduce MCT back to Navier-Stokes equations.

2.1 Kinetic Theory for Morphing Continuum at Equilibrium

The Boltzmann equation and kinetic theory have been considered as the fundamental equations of hydrodynamics and combine atomic-level physics with statistical averaging. It is well known that the Navier-Stokes equations can be deduced from kinetic theory and the Boltzmann equations using a first order approximation. However, it should be emphasized that the original Bolzmann equation and kinetic theory are based on a monatomic particle assumption. Therefore, more ad hoc approximations have to be made for diatomic or polyatomic molecular gases. Assuming the dynamics of the collisions do not depend on the vibrational energy, Curtiss extended the original formulations for the Boltzmann equation and found the generalized Boltzmann equation (Boltzmann-Curtiss equation) as [23, 24]

$$\begin{aligned} \bar{f}\left(\mathbf{x},\mathbf{p},\boldsymbol{\phi},\mathbf{M},t\right) &= \int f\left(\mathbf{x},\mathbf{p},\boldsymbol{\phi},\mathbf{M},E_{\mathrm{vib}},\tau,t\right) dE_{\mathrm{vib}} d\tau, \\ \left(\frac{\partial}{\partial t}+\frac{\mathbf{p}}{m}\frac{\partial}{\partial \mathbf{x}}+\frac{\mathbf{M}}{I}\frac{\partial}{\partial \boldsymbol{\phi}}\right)\bar{f} &= \sum_{\beta}\mathbf{Z}_{\beta}, \end{aligned} \tag{1}$$

where $\mathbf{x}$ is the position, $\mathbf{p}$ the linear momentum, $\boldsymbol{\phi}$ the orientation, $\mathbf{M}$ the angular momentum, $\mathbf{Z}$ the collision integral integrated over β molecules that interact with a given molecule, and I the moment of inertia. It should be noted that Curtiss did not provide a distribution function for the Boltzmann-Curtiss equations. This study presents a distribution that works well with the Boltzmann-Curtiss equations.

Let χ be any conserved kinetic variable associated with a molecule of velocity $\mathbf{v}$ and angular velocity $\boldsymbol{\omega}$ located at $\mathbf{x}$, such that in any collision at $\mathbf{x}$ one has $\{\mathbf{p}_1,\boldsymbol{\omega}_1,\mathbf{p}_2,\boldsymbol{\omega}_2\} \rightarrow \{\mathbf{p}_1',\boldsymbol{\omega}_1',\mathbf{p}_2',\boldsymbol{\omega}_2'\}$ so that $\chi_1+\chi_2=\chi_1'+\chi_2'$ where $\chi_1=\chi(\mathbf{x}_1,\mathbf{p}_1,\boldsymbol{\omega}_1)$. The conservation theorem relevant to the Boltzmann-Curtiss equation can be obtained by multiplying Eq. 1 on both sides by χ and integrating over $\mathbf{v}'$ and $\boldsymbol{\omega}'$. The collision term vanishes and the average value, $\langle A\rangle$, is obtained as

$$\langle A\rangle \equiv \frac{\int d^3\,\mathbf{v}' d^3\boldsymbol{\omega}' A\bar{f}}{\int d^3\mathbf{v}'\,d^3\boldsymbol{\omega}'\bar{f}} = \frac{1}{n}\int d^3\mathbf{v}'\,d^3\boldsymbol{\omega}' A\bar{f}, \tag{2}$$

where $n(\mathbf{x},t)\equiv\int d^3\,\mathbf{v}' d^3\boldsymbol{\omega}'\bar{f}(\mathbf{x},\mathbf{p},\boldsymbol{\omega},t)$.

Assume the inner structure as a rigid sphere and has no distribution inside the molecule, i.e. $\frac{\partial}{\partial\phi_k}=0$. In the absence of body force and couple moment,

the conservation equation is

$$\frac{\partial}{\partial t}\langle n\chi\rangle + \frac{\partial}{\partial x_i}\langle n\chi v_i\rangle - n\langle v_i\frac{\partial \chi}{\partial x_i}\rangle + \frac{\partial}{\partial \phi_i}\langle n\chi\omega_i\rangle - n\langle\omega_i\frac{\partial\chi}{\partial\phi_i}\rangle = 0,$$
$$\Rightarrow \frac{\partial}{\partial t}\langle n\chi\rangle + \frac{\partial}{\partial x_i}\langle n\chi v_i\rangle - n\langle v_i\frac{\partial \chi}{\partial x_i}\rangle = 0 \tag{3}$$

The Boltzmann-Curtiss distribution is

$$\bar{f}\left(\mathbf{x},\mathbf{v},\boldsymbol{\omega}\right) = n\left(\frac{m\sqrt{j}}{2\pi k\theta}\right)^3 \exp\left[-\frac{m(\mathbf{v}'^2 + j\boldsymbol{\omega}'^2)}{2k\theta}\right]. \tag{4}$$

The corresponding probability density function has the proper normalization, i.e.,

$$\int_{-\infty}^{\infty}\left(\frac{m\sqrt{j}}{2\pi k\theta}\right)^3 \exp\left[-\frac{m(\mathbf{v}'^2 + j\boldsymbol{\omega}'^2)}{2k\theta}\right] d^3\mathbf{v}\, d^3\boldsymbol{\omega} = 1. \tag{5}$$

Here m is the mass of the molecule, j is the microinertia for the inner structure and k is the Boltzmann constant. One can understand microinertia through the concept of moment of inertia. Microinertia is a measurement of the resistance of the internal structure to changes to its rotation and can be defined as

$$j \equiv 2\langle r_m r_m\rangle = 2\frac{\int_{\Delta v'}\rho' r_m r_m dv'}{\int_{\Delta v'}\rho' d'_v},$$

where r_m is the local coordinate from the centroid of the internal structure and $\Delta v'$ is the volume of the inner structure.

It should be noted that following the equipartition of energy, $E_{\text{int}} = \frac{1}{2}N_{\text{DOF}}nk\theta$, the internal energy can be shown to be

$$E_{\text{int}} = \frac{6}{2}nk\theta = \frac{1}{2}m\left(\langle\mathbf{v}'^2\rangle + j\langle\boldsymbol{\omega}'^2\rangle\right), \tag{6}$$

where N_{DOF} is the number of the degrees of freedom in a polyatomic molecule and n is the number of the molecules in the system. The velocity v_i and the angular velocity ω_i can be decomposed as $v_i = U_i + v'_i$ and $\omega_i = W_i + \omega'_i$.

The equations for fluid dynamics involving particles with inner structure can be derived by calculating the moments of the Boltzmann-Curtiss equations for quantities that are conserved in collisions of the molecules. There are four conserved quantities χ, i.e., the mass $\chi_1 = m$, the total linear momentum $\chi_2 = mv_i^* = m(v_i + e_{ijk}\omega_j r_k)$, the angular momentum $\chi_3 = mj\omega_m$ and the total energy $\chi_4 = \frac{1}{2}m(v_i v_i + j\omega_i\omega_j)$.

If $\chi_1 = m$ is chosen and inserted into Eq. 3, one obtains

$$\frac{\partial}{\partial t}\langle nm\rangle + \frac{\partial}{\partial x_i}\langle nmv_i\rangle = 0, \tag{7}$$

With $nm = \rho$ and $\langle v_i\rangle = U_i$, the continuity equation is obtained as

$$\frac{\partial}{\partial t}\rho + \frac{\partial}{\partial x_i}\left(\rho U_i\right) = 0. \tag{8}$$

If $\chi_2 = mv_i^* = m(v_i + e_{ijk}\omega_j r_k)$, Eq. 3 becomes

$$\frac{\partial}{\partial t}\langle nmv_j\rangle + \frac{\partial}{\partial t}(nme_{jmn}\omega_m r_n) + \frac{\partial}{\partial x_i}\langle nmv_i v_j\rangle + \frac{\partial}{\partial x_i}\langle nme_{jmn}\omega_m r_n v_i\rangle = 0, \tag{9}$$

or

$$\frac{\partial}{\partial t}(\rho U_j) + \frac{\partial}{\partial x_i}(\rho U_i U_j) = -\frac{\partial}{\partial x_i}\left(\rho\langle v_i' v_j'\rangle + \rho e_{jmn} r_n \langle v_i'\omega_m'\rangle\right). \tag{10}$$

Here $U_j^* = U_j + e_{jmn}W_m r_n$ is the total averaged velocity with the fluctuating velocity integrated over the volume of the molecule being zero.The quantity $t_{ij}^{\text{Boltzmann}} = \rho\langle v_i' v_j'\rangle$ is the stress similar to that in the classical Boltzmann equation and $t_{ij}^{\text{Curtiss}} = \rho e_{jmn} r_n \langle v_i'\omega_m'\rangle$ is the asymmetric part of the stress due to the rotation discussed by Curtiss [24], Eringen [4, 26], Stokes [75] and others [16]. It should be noticed that the integral for the symmetric part of the stress, $t_{ij}^{\text{Boltzmann}}$, is different from the one in the classical Boltzmann equation due to the distribution function used; however, the derivation still yields the gas pressure and the classical symmetric stress tensor at Boltzmann-Curtiss distribution, namely

$$\begin{aligned} t_{ij}^{\text{Boltzmann}} &= p\delta_{ij} - t_{ij}^{\text{Boltzmann,viscous}} = \rho\langle v_i' v_j'\rangle \\ &= \frac{\rho}{n}\iint n v_i' v_j' \left(\frac{m(j)^{\frac{1}{2}}}{2\pi k\theta}\right)^3 e^{-\frac{m\left(\mathbf{v'}^2 + j\boldsymbol{\omega'}^2\right)}{2k\theta}} d^3\mathbf{v'}\, d^3\boldsymbol{\omega'}. \end{aligned} \tag{11}$$

It is also straightforward to prove that $\rho\langle v_x' v_x'\rangle = \rho\langle v_y' v_y'\rangle = \rho\langle v_z' v_z'\rangle = nk\theta$ and define the gas pressure as $p \equiv \frac{1}{3}\rho\langle \mathbf{v'}^2\rangle$ when the system is at the Boltzmann-Curtiss distribution.

For a rotating body, one of the important quantities is angular momentum. Therefore, the third kinetic variable is $\chi_3 = mj\omega_m$, where j is the inertia of the subscale sturcture. With the substitution of χ_3, Eq. 3 becomes

$$\frac{\partial}{\partial t}\langle nmj\omega_m\rangle + \frac{\partial}{\partial x_i}\langle nmj\omega_m v_i\rangle = 0$$

or

$$\frac{\partial}{\partial t}(\rho j W_m) + \frac{\partial}{\partial x_i}(\rho j W_m U_i) = -\frac{\partial}{\partial x_i}(\rho j\langle\omega_m' v_i'\rangle), \tag{12}$$

where the right-hand term, $m_{im} = \rho j\langle\omega_m' v_i'\rangle$, is the combination of the moment stress due to rotation and the asymmetric part of the Cauchy stress, $t_{ij}^{\text{Curtiss}} = \rho e_{jmn} r_n \langle v_i'\omega_m'\rangle$.

In classical kinetic theory, the internal energy density is defined as $e = \frac{1}{2}\langle v_m' v_m'\rangle$; however, because of the rotating effect of the molecule, the internal energy density should be re-defined as $e = \frac{1}{2}(\langle v_m' v_m'\rangle + j\langle\omega_m'\omega_n'\rangle)$. Similarly, the total energy is classically defined as $\frac{1}{2}m(v_m v_m)$, but due to the rotation effects of the molecule it should now be defined as $\frac{1}{2}m(v_m v_m + j\omega_m\omega_m)$. This can also be stated as $\frac{1}{2}m(e + U_m U_m + jW_m W_m)$. After inserting the last kinetic variable,

i.e., total energy, $\chi_4 = \frac{1}{2}m(v_m v_m + j\omega_m\omega_m)$, Eq. 3 is now

$$\begin{aligned}
&\frac{\partial}{\partial t}(\rho e) + \frac{\partial}{\partial x_i}(\rho e U_i) \\
&\quad = U_m \frac{\partial}{\partial x_i}\left(\rho e_{mjn} r_n \langle v_i' \omega_j' \rangle\right) - \rho \langle v_i' v_m' \rangle \frac{\partial U_m}{\partial x_i} \\
&\quad - \frac{\partial}{\partial x_i}\left(\frac{1}{2}\rho\left(\langle v_m' v_m' v_i' \rangle + j\langle \omega_m' \omega_n' v_i' \rangle\right)\right) - \rho j \langle \omega_m' v_i' \rangle \frac{\partial W_m}{\partial x_i},
\end{aligned} \tag{13}$$

or

$$\begin{aligned}
&\frac{\partial}{\partial t}(\rho e) + \frac{\partial}{\partial x_i}(\rho e U_i) \\
&\quad = t_{im,i}^{\text{Curtiss}} U_m - t_{im}^{\text{Boltzmann}} U_{m,i} - q_{i,i} - m_{im} W_{m,i}.
\end{aligned} \tag{14}$$

It should be noted that because of the molecular rotation, the heat flux density has an additional term involving rotation and is now defined as $q_i = \frac{1}{2}\rho(\langle v_m' v_m' v_i' \rangle + j\langle \omega_m' \omega_n' v_i' \rangle)$.

If the mean free path is small compared to other characteristic lengths, the system rapidly comes to a local equilibrium. In classical kinetic theory, it is well known that the zero-order approximation reduces the Boltzmann equations to the governing equations for inviscid flow (i.e., Euler equations). Here, the zero-order approximation is applied to the Boltzmann-Curtiss equations. First assume that the gas has a local Boltzmann-Curtiss distribution, with slowly varying temperature, density, velocity and rotation, so the distribution can be approximated by

$$\bar{f}(\mathbf{x}, \mathbf{v}, \boldsymbol{\omega}) \approx \bar{f}^0(\mathbf{x}, \mathbf{v}, \boldsymbol{\omega}) = n\left(\frac{m\sqrt{j}}{2\pi k\theta}\right)^3 \exp\left[-\frac{m(\mathbf{v}'^2 + j\boldsymbol{\omega}'^2)}{2k\theta}\right] \tag{15}$$

It should be noted that the Boltzmann-Curtiss distribution is not the exact solution to Eq. 1; however, it serves as a reasonable approximation just as the Maxwell-Boltzmann distribution serves as a good approximation for classical kinetic theory. In the previous section, it has already been shown that $\langle v_i' v_i' \rangle = 3nk\theta$ and consequently, the pressure becomes

$$\begin{aligned}
t_{ij}^{\text{Boltzmann},0} &= P_{ij}^0 \\
&= \frac{\rho}{n} \iint n v_i v_j \left(\frac{m\sqrt{j}}{2\pi k\theta}\right)^3 \exp\left[-\frac{m(\mathbf{v}'^2 + j\boldsymbol{\omega}'^2)}{2k\theta}\right] d^3\mathbf{v}' d^3\boldsymbol{\omega}' \\
&= nk\theta\delta_{ij}.
\end{aligned} \tag{16}$$

In addition, it is straightforward to prove that

$$\begin{aligned}
t_{ij}^{\text{Curtiss},0} &= \frac{\rho}{n} e_{jmn} r_n \iint n v_i' \omega_m' \left(\frac{m\sqrt{j}}{2\pi k\theta}\right)^3 \exp\left[-\frac{m(\mathbf{v}'^2 + j\boldsymbol{\omega}'^2)}{2k\theta}\right] d^3\mathbf{v}' d^3\boldsymbol{\omega}' = 0, \\
m_{ij}^0 &= \frac{\rho}{n} j \iint n \omega_m' v_i' \left(\frac{m\sqrt{j}}{2\pi k\theta}\right)^3 \exp\left[-\frac{m(\mathbf{v}'^2 + j\boldsymbol{\omega}'^2)}{2k\theta}\right] d^3\mathbf{v}' d^3\boldsymbol{\omega}' = 0, \\
q_i^0 &= \frac{\rho}{2n} \iint n(v_m' v_m' v_i' + j\omega_m' \omega_n' v_i') \left(\frac{m\sqrt{j}}{2\pi k\theta}\right)^3 \exp\left[-\frac{m(\mathbf{v}'^2 + j\boldsymbol{\omega}'^2)}{2k\theta}\right] d^3\mathbf{v}' d^3\boldsymbol{\omega}' = 0.
\end{aligned} \tag{17}$$

With these results, the transport equations become

$$\begin{aligned}
&\frac{\partial}{\partial t}\rho + \frac{\partial}{\partial x_i}\left(\rho U_i\right) = 0, \\
&\frac{\partial}{\partial t}\left(\rho U_j\right) + \frac{\partial}{\partial x_i}\left(\rho U_i U_j\right) = -\frac{\partial}{\partial x_i}\left(nk\theta\delta_{ij}\right), \\
&\frac{\partial}{\partial t}\left(\rho j W_m\right) + \frac{\partial}{\partial x_i}\left(\rho j W_m U_i\right) = 0, \\
&\frac{\partial}{\partial t}\left(\rho e\right) + \frac{\partial}{\partial x_i}\left(\rho e U_i\right) = -nk\theta U_{i,i}
\end{aligned} \tag{18}$$

2.2 First-order Boltzmann-Curtiss Equations

Researchers have been heavily relying on vorticity to characterize the flow physics of vortices, eddies and molecular rotations [53]. However, vorticity-based descriptions are often found inadequate or inconsistent when the vorticity field deviates from local rotations [35]. Those cases are considered as flows with strong local spins. It should be emphasized that spin is different from vorticity. Vorticity is defined by curl of velocity. In other words, it is a consequent motion of the translation. On the other hand, spin can be an independent motion. One could use the solar system as an example. Each planet spins on its own axis while moving on its own orbits. The translational veocities of any two planets are used to calculate their corresponding vorticity; however, such quantity does not represent the spinning of either planets.

Flows with strong local spin have been the focus of extensive theoretical, experimental, and numerical work for decades [26, 38, 41, 43, 60, 81]. High-speed, turbulent, compressible, reacting, and polyatomic gas flows all involve complex interactions based on strong local spin. The Wang Chan-Uhlenbeck equation accounts for molecular spin through the lens of quantum mechanics, treating each different quantum state as a separate species of molecule [83]. This additional rigor adds more complexity to the distribution function and the dynamics of the collision integral. For classical physics, however, local rotation may affect the dynamics of the entire flow. Turbulent flows, in particular, may produce additional angular momentum from the smallest eddies. The rotation of these smallest eddies affects the energy and momentum transfer at the inertial length scales, requiring researchers to develop methods that capture this additional small-scale angular momentum. The most effective of these analytical methods have revealed deeper physical or mathematical characteristics to previously well-tested theories of fluid dynamics [1, 26, 27, 28, 45, 76].

For monatomic gases composed of infinitesimal particles, any kinetic theory needs to track only the position and translational velocity of the particles. These assumptions greatly simplify the probability distribution of particles, as well as the transport equation used to describe the evolution of that distribution. When the particles are given a finite size and allowed to rotate, additional motions bring additional degrees of freedom to the system. If the angular motion of the particles is independent from the translational motion and is dependent on its orientation, then the transport equation has the form [15, 24]:

$$\left(\frac{\partial}{\partial t} + \frac{p_i}{m}\frac{\partial}{\partial x_i} + \frac{M_i}{I}\frac{\partial}{\partial \Phi_i}\right) f = \left(\frac{\partial f}{\partial t}\right)_{coll} \tag{19}$$

Here m denotes the mass of a particle, p_i represents the linear momentum, M_i the angular momentum, I the moment of inertia of a particle, and Φ_i the Euler angle with respect to the center of mass of the particle.

The solution $f(p_i, \Phi_i, x_i, t)$ gives the probability a particular particle will possess the values of the given variables, and generalizes the motion of the system by simplifying the interactions of individual particles. For instance, this solution is absent of dependencies on vibrational energy or vibrational motion, as the dynamics of individual collisions are assumed to be independent of these variables. The right-hand side of equation 19 accounts for the cumulative effect of collisons on the distribution. For this description, the particles are treated as spheres, so all axial orientations of the distribution are equivalent, i.e. independent of the Euler angle. Therefore, the Boltzmann-Curtiss transport equation becomes:

$$(\frac{\partial}{\partial t} + \frac{p_i}{m}\frac{\partial}{\partial x_i})f = (\frac{\partial f}{\partial t})_{coll} \tag{20}$$

Equilibirum solutions to this equation should look similar to the Maxwell-Boltzmann distribution function, as the remaining terms are concerned with linear momentum. Still, the presence of an independent angular rotation, ω_i, changes the distribution of kinetic energy of the particles. From Boltzmann's principle, the equilibrium solution to equation 20 can be approximated as [14]:

$$f^0(x_i, v_i, \omega_i, t) = \ n(\frac{\sqrt{mI}}{2\pi\theta})^3 \ exp(-\frac{m(v_l'v_l') + I(\omega_p'\omega_p')}{2\theta}) \tag{21}$$

Here, the perturbed velocity, $v_l' = v_l - U_l$, for mean velocity U_l and the perturbed gyration, $\omega_p' = \omega_p - W_p$ for mean gyration W_p, are introduced. The form of this distribution function differs from the classical Boltzmann distribution function [46, 77], which assigns a 3/2 power to the terms in front of the exponential. The increased exponential in equation 21 arises due to the additional contribution to the momentum by the gyration, ω_p'. The number density, n, of the particles is found by integrating the distribution function f over all the perturbed variables, $\mathbf{v}'$ and ω', which is now a six-dimensional integral:

$$n = \int\int d^3v' d^3\omega' f^0 \tag{22}$$

The superscript indicates that this function only serves as a zeroth-order approximation to the true solution. In equation 21, the mean thermal energy θ, mean velocity and mean gyration are assumed to vary slowly in time due to the rapid number of collisions, ensuring a rapid return to equilibrium. The thermal energy, $\theta = kT$, contains the Boltzmann constant k and absolute temperature T. Classical kinetic approaches by Huang [39] and by Gupta et al for granular fluids [34] often group the Boltzmann constant with the characteristic temperature to focus on the thermal energy of the system. The velocity and gyration perturbations represent the rapid fluctuations of the spheres, and provide the main source of any dynamics at equilibrium. Furthermore, the moment of inertia of a sphere can be expressed in terms of a parameter j [18], known as the microinertia. This parameter comes from the averaging of spatial coordinates attached to the sphere, allowing one to show that $j = \frac{2}{5}d^2$, where d is the diameter of the sphere [18]. Substituting $I = mj$ into equation 21 yields:

$$f^0(x_i, v_i, \omega_i, t) = n(\frac{m\sqrt{j}}{2\pi\theta})^3 exp(-\frac{m(v_l'v_l' + j\omega_p'\omega_p')}{2\theta}) \tag{23}$$

This equilibrium distribution function represents the starting point for the kinetic theory derivation, providing an abstract description of the system. To account for the evolution of the physical motion of a particle, the balance laws must be derived. The average of a quantity A is here defined by the following expression:

$$\langle A \rangle = \frac{1}{n} \int \int A f(x_i, v_i, \omega_i, t) d^3v' d^3\omega' \tag{24}$$

where n is the number density of the particles and is found by integrating the distribution function f over all the perturbed variables, $\mathbf{v}'$ and ω'. The mean velocity and gyration are naturally obtained from $\langle \mathbf{v} \rangle$ and $\langle \omega \rangle$. Therefore, any balance laws governing the mean velocity and mean gyration must come by averaging the transport equation 20 for some conserved quantity $\chi(x_i, p_i)$:

$$\frac{\partial}{\partial t}\langle n\chi \rangle + \frac{\partial}{\partial x_i}\langle n\frac{p_i}{m}\chi \rangle - n\langle \frac{p_i}{m}\frac{\partial \chi}{\partial x_i} \rangle = 0 \tag{25}$$

Note that all potential time derivatives vanished as χ is a function of momentum and position alone. The collisional term emerging from the averaging of the right-hand side of equation 20 is also presumed to vanish, namely, $\langle \chi(x_i, p_i)(\frac{\partial f}{\partial t})_{coll} \rangle = 0$. Huang proved this statement for any conserved quantity [39], and his proof will be discussed with the effects of collisions in more detail.

The balance laws come by letting χ equal the conserved values of mass m, linear momentum $m(v_i + \epsilon_{ipl} r_l \omega_p)$, angular momentum $m r_i r_p \omega_p$ and total energy $m(e + \frac{1}{2} v_l' v_l' + r_p r_q \omega_p' \omega_q')$. The new velocity associated with the linear momentum arises from the combined motion of the classical translational velocity, v_i, and the contribution of the gyration to the total velocity, $\epsilon_{ipl} r_l \omega_p$ [30]. The angular momentum is the standard expression involving the the cross product of the local angular velocity induced by the gyration, $r_p \omega_p$, and the radial coordinate emerging from the center of mass of the particle, r_i.

Finally, the conserved quantity of energy contains the kinetic energy associated with the local angular velocity, $r_n \omega_n$, and adds this to the traditional translational kinetic energy. Substituting the conserved quantities of mass, linear momentum, angular momentum, and energy for χ into the conservation equation 25 and letting the averages of the variables equal their mean values and splitting total variables into mean and fluctuating components, the balance laws become:

Continuity

$$\frac{\partial}{\partial t}\rho + \frac{\partial}{\partial x_l}(\rho U_l) = 0 \tag{26}$$

Linear Momentum

$$\frac{\partial}{\partial t}(\rho U_s) + \frac{\partial}{\partial x_l}(\rho U_s U_l) + \frac{\partial}{\partial x_l}(\rho\langle v_s' v_l'\rangle + \langle \rho\epsilon_{spq} v_l' r_q \omega_p'\rangle) = 0 \tag{27}$$

Angular Momentum

$$\frac{\partial}{\partial t}(\rho i_{sp} W_p) + \frac{\partial}{\partial x_l}(\rho i_{sp} W_p U_l) + \frac{\partial}{\partial x_l}(\rho\langle i_{sp}\omega_p' v_l'\rangle) = 0 \tag{28}$$

Energy

$$\frac{\partial}{\partial t}(\rho e) + \frac{\partial}{\partial x_l}(\rho e U_l) + \frac{\partial}{\partial x_l}\frac{1}{2}\langle \rho v_s' v_s' v_l' + i_{pq}\omega_q'\omega_p' v_l'\rangle - \rho\langle v_l \frac{\partial e}{\partial x_l}\rangle = 0 \tag{29}$$

Here, the properties $\langle v'\chi\rangle = 0$ and $\langle \omega'\chi\rangle = 0$ are employed. Additionally, the term $\langle \epsilon_{ipl} v_s r_l W_p\rangle = 0$ as this can be viewed as an integral of the fluctuating component of the total velocity [6, 14]. Also, the term $i_{pq} = r_p r_q$ is used to represent the product of the coordinates, r_p, emerging from the center of mass of the particle. These coordinates measure the relative deformation of a particle, tracking how the surface varies about the center of mass. The tensor i_{pq} is related to the earlier parameter j, known as the microinertia. For spherical particles, i_{pq} is reduced to $i_{pq}\delta_{pq} = i_{pp}$, which can be shown to equal $\frac{3j}{2}$ [18]. Applying this reduction to i_{pq} the balance laws become:

Continuity

$$\frac{\partial}{\partial t}\rho + \frac{\partial}{\partial x_l}(\rho U_l) = 0 \tag{30}$$

Linear Momentum

$$\frac{\partial}{\partial t}(\rho U_s) + \frac{\partial}{\partial x_l}(\rho U_s U_l) + \frac{\partial}{\partial x_l}(\rho\langle v_s' v_l'\rangle + \langle \rho\epsilon_{spq} v_l' r_q \omega_p'\rangle) = 0 \tag{31}$$

Angular Momentum

$$\frac{\partial}{\partial t}(\frac{3\rho j W_s}{2}) + \frac{\partial}{\partial x_l}(\frac{3\rho j W_s U_l}{2}) + \frac{\partial}{\partial x_l}\rho\langle\frac{3j\omega_s' v_l'}{2}\rangle = 0 \tag{32}$$

Energy

$$\frac{\partial}{\partial t}(\rho e) + \frac{\partial}{\partial x_l}(\rho e U_l) + \frac{\partial}{\partial x_l}\frac{1}{2}\langle \rho v_s' v_s' v_l' + \frac{3j\omega_p'\omega_p' v_l'}{2}\rangle - \rho\langle v_l \frac{\partial e}{\partial x_l}\rangle = 0 \tag{33}$$

These conservation equations feature material derivatives for the mean flow variables as well as gradients of products of perturbed variables. These perturbations are variables in the distribution function, and so can be treated separately.

Defining these expressions in the following way:

$$q_\alpha = \frac{1}{2}\langle \rho v_l' v_l' v_\alpha' + \frac{3j\omega_p'\omega_p' v_\alpha'}{2} \rangle \tag{34}$$

$$t_{\alpha\beta}^{\text{Bol}} = -\rho\langle v_\alpha' v_\beta' \rangle \tag{35}$$

$$t_{\alpha\beta}^{\text{Cur}} = -\rho\langle v_\alpha' \epsilon_{\beta pq} r_q \omega_p' \rangle \tag{36}$$

$$m_{\alpha\beta} = -\rho\langle \frac{3j\omega_\beta' v_\alpha'}{2} \rangle \tag{37}$$

Here, q_α denotes the heat flux, $t_{\alpha\beta}^{\text{Bol}}$ gives the Boltzmann stress, $t_{\alpha\beta}^{\text{Cur}}$ yields the Curtiss stress, and $m_{\alpha\beta}$ introduces the moment stress. Plugging these expressions into the balance laws gives:

Continuity

$$\frac{\partial}{\partial t}\rho + \frac{\partial}{\partial x_l}(\rho U_l) = 0 \tag{38}$$

Linear Momentum

$$\frac{\partial}{\partial t}(\rho U_s) + \frac{\partial}{\partial x_l}(\rho U_s U_l) - \frac{\partial}{\partial x_l}(t_{ls}^{\text{Bol}} + t_{ls}^{\text{Cur}}) = 0 \tag{39}$$

Angular Momentum

$$\frac{\partial}{\partial t}(\rho j W_s) + \frac{\partial}{\partial x_l}(\rho j W_s U_l) - \frac{2}{3}\frac{\partial}{\partial x_l}(m_{ls}) = 0 \tag{40}$$

Energy

$$\frac{\partial}{\partial t}(\rho e) + \frac{\partial}{\partial x_l}(\rho e U_l) + \frac{\partial q_l}{\partial x_l} - \rho\langle v_l \frac{\partial e}{\partial x_l} \rangle = 0 \tag{41}$$

Indeed, the expressions 34, 35, 36, and 37 refer to familiar stresses that require a more detailed treatment. At the moment, they represent only source or sink terms for the momentum and energy of the flow. These terms can be determined from the definition of the average in equation 24 using the equilibrium distribution in equation 23, which would give a very rough approximation of how they contribute to the balance laws. A more thorough treatment of their contribution, however, requires the derivation of a distribution function that accounts for departures in the fluid from equilibrium. For this function, the Chapman-Enskog process is followed to derive a first order approximation to the solution of the Boltzmann transport equation 20.

The right-hand side of the transport equation 20 tracks the gain or loss of particles due to collisions in some small time interval. For the equilibrium distribution function in equation 23, the assumption was made that a large number of binary collisions occurred over a short time interval, meaning that any deviation from equilibrium would result in a rapid return to equilibrium. These binary collisions affect the initial rotation and velocity of the particle instantaneously at the moment the particles collide. Huang studied these binary collisions considering molecules with only translational velocities [39]. The existence of spin within molecules was treated through the lens of quantum mechanics, denoting different spin states as separate species of molecules. In order to account for these different spins, then, one would need to solve the Wang Chang-Uhlenbeck equation [83] for the distribution function of each of these molecular species, with a collisional integral that accounts for the cross-section calculated from

the quantum states of these species. Here, the Boltzmann-Curtiss distribution function described in equation 23 treats gyration as an additional classical variable applicable to the same molecules throughout the domain, thus requiring only one solution to describe the distribution of rotation throughout the system. Additionally, the collisional integral is easier to calculate since the rotational motion is treated as a classical motion.

The collision rate on the right-hand side of the Boltzmann transport equation 20 is given by the following integral:

$$(\frac{\partial f}{\partial t})_{coll} = \int d^3p_2 \; d^3p_1' \; d^3p_2' \; \delta^4(P_f - P_i) \, |T_{fi}|^2 \, (f_2' f_1' - f_2 f_1) \tag{42}$$

Here, P_f and P_i refer to the total final and initial momenta, p_1 and p_2 refer to the initial momenta of the colliding particles while their primed counterparts, p_1' and p_2' each refer to their respective final linear momentum. As mentioned previously, these linear momenta contain an added term to the classical linear momentum, $p_i = mv_i$, found in the Boltzmann transport equation. Here, the Boltzmann-Curtiss linear momentum, $p_i = m(v_i + \epsilon_{ipl} r_l \omega_p)$, includes an additional contribution from the component of the local rotation moving in the direction of the translational velocity. The transition matrix T_{fi} contains the elements of the operator $T(E)$ that converts the particle from its initial to final state in the collision. Finally the distribution functions f_1 and f_2 refer to the distributions of particles containing momenta p_1 and p_2 respectively while the primed distribution functions contain the final momenta values denoted by the primed counterparts p_1' and p_2'. Any conserved quantity for a particle initiating a binary collision, χ, integrated with the collision integral 42 vanishes. Huang proved this result by interchanging the momenta variables before and after the collision and integrating over pre-collision and post-collision linear momenta [39]. When equation 42 is used on the right-hand side of the Boltzmann-Curtiss transport equation 20, the Wang Chan-Uhlenbeck equation is obtained [83]:

$$(\frac{\partial}{\partial t} + \frac{p_i}{m}\frac{\partial}{\partial x_i})f = \int d^3p_2 \; d^3p_1' \; d^3p_2' \; \delta^4(P_f - P_i) \, |T_{fi}|^2 \, (f_2' f_1' - f_2 f_1) \tag{43}$$

This treatment will look at a simplified version of this equation.

In observing the effect of collisions on equation 43, it is important to recognize that $(\frac{\partial f^0}{\partial t})_{coll} = 0$ for the equilibrium Boltzmann-Curtiss distribution function defined in equation 23. This result emerges from the fact that the coefficients in equation 23 do not depend on the velocity v_i [39]. To get a good approximation of the collision integral 42, higher order approximations of f are needed. If the distribution function g is defined by the expression:

$$g(x_i, p_i, t) = f(x_i, p_i, t) - f^0(x_i, p_i, t) \tag{44}$$

then the collision integral, e.g. equation 42, can be approximated with the following expression:

$$\begin{aligned}(\frac{\partial f}{\partial t})_{coll} \; \approx \; & \int d^3p_2 \; d^3p_1' \; d^3p_2' \; \delta^4(P_f - P_i) |T_{fi}|^2 \\ & (f_2^{0'} g_1' - f_2^0 g_1 + g_2' f_1^{0'} - g_2 f_1^0)\end{aligned} \tag{45}$$

where squared terms involving g have been neglected due to their presumed smaller magnitude in relation to f^0. Indices associated with different distri-

bution functions again correspond to the initial and final distributions of the particles in the binary collisions. To assess the relative magnitude of the terms within equation 45, the second term on the right-hand side can be calculated by the expression:

$$-g_1(\mathbf{x}, \mathbf{p}_1, t) \int d^3p_2 \; d^3p_1' \; d^3p_2' [\delta^4(P_f - P_i) \left|T_{fi}\right|^2 f_2^0 = -\frac{g_1}{\tau} \tag{46}$$

Here, the time constant τ incorporates all the physics associated with the transition from initial to final states, including the transfer of angular momentum through the new variable of gyration. A more in-depth treatment of the gyration and the characteristic time constants associated with its evolution will be given in the later part of the report.

Given the order-of-magnitude estimate to the collision integral 45, the right-hand side of the Boltzmann transport equation can be given a simpler treatment with the expression:

$$(\frac{\partial f}{\partial t})_{coll} = -\frac{f - f^0}{\tau} = -\frac{g}{\tau} \tag{47}$$

The first-order distribution function, g, measures the probability that large numbers of particles will exit their equilibrium state purely through collisions. The time constant τ now gives an approximation for the entire distribution departing from equilibrium through collisions. Therefore, this time constant should characterize the transition of all degrees of freedom to and from their equilibrium states. If the time-scale of the problem is reduced such that only one motion departs from equilibrium, as Parker considered for internal rotation [57], then this time constant can be scaled to focus on this relaxation process. If further approximations are needed to account for additional physics, the relaxation time can be expanded into a series of terms that take into account these additional interactions. Chen et al applied this approach [13] to generate an expression for the characteristic collision time scale of turbulent eddy interactions. Such expansions have the benefit of incorporating multiple physical processes within one time constant, allowing for the interaction of rotation and translation to affect the relaxation of the distribution function simultaneously.

If equation 47 is substituted into the transport equation 20, an approximate form of the transport equation known as the Bhatnagar, Gross, and Krook (BGK) equation is obtained [7]:

$$g = -\tau(\frac{\partial}{\partial t} + v_i \frac{\partial}{\partial x_i})(f^0 + g) \tag{48}$$

Since g measures the probability of large numbers of particles deviating from their equilibrium state, its relative magnitude to f^0 matters greatly in terms of what kind of system is being described. For this paper, it suffices to show what forces and properties are influencing the mean flow when slight deviations to equilibrium occur. Therefore, it can be assumed that $g << f^0$, reducing equation 48 to the form:

$$g = -\tau(\frac{\partial}{\partial t} + v_i \frac{\partial}{\partial x_i}) f^0 \tag{49}$$

This equation gives a formula for finding g entirely in terms of derivatives of f^0. Still, the variables in the transport equation 49 are present in f^0 only through

its independent variables. Therefore, to get the spatial derivates of f^0, the following derivatives of its independent variables are calculated:

$$\frac{\partial f^0}{\partial \rho} = \frac{f^0}{\rho} \tag{50}$$

$$\frac{\partial f^0}{\partial \theta} = -(3 - \frac{m(v'^2 + j\omega'^2)}{2\theta})\frac{f^0}{\theta} \tag{51}$$

$$\frac{\partial f^0}{\partial U_i} = \frac{mv_i'}{\theta} f^0 \tag{52}$$

$$\frac{\partial f^0}{\partial W_i} = \frac{mj\omega_i'}{\theta} f^0 \tag{53}$$

Using the chain rule, the expression for g in equation 49 can be written as:

$$\begin{aligned} g = -\tau f^0 (\frac{1}{\rho} D(\rho) + \frac{1}{\theta}(\frac{m(v'^2 + j\omega'^2)}{2\theta} - 3) D(\theta) + (\frac{mv_i'}{\theta}) D(U_i) \\ + (\frac{mj\omega_i'}{\theta}) D(W_i)) \end{aligned} \tag{54}$$

where $D(X) = (\frac{\partial}{\partial t} + v_i \frac{\partial}{\partial x_i})X$. The material derivatives present in equation 54 can be derived from the zeroth order balance laws. To obtain the zeroth order approximations of the equations 38, 39, 40, 41, the terms related to the perturbation of the velocity and gyration are eliminated, yielding:

$$\frac{\partial \rho}{\partial t} + \frac{\partial \rho U_l}{\partial x_l} = 0 \tag{55}$$

$$\frac{\partial}{\partial t}(\rho U_s) + \frac{\partial}{\partial x_l}(\rho U_l U_s) = -\frac{\partial}{\partial x_s}(n\theta) \tag{56}$$

$$\frac{\partial}{\partial t}(\rho j W_s) + \frac{\partial}{\partial x_l}(\rho j W_s U_l) = 0 \tag{57}$$

$$\frac{\partial}{\partial t}(n\theta) + \frac{\partial}{\partial x_l}(n\theta U_l) = -\frac{n\theta}{3}\frac{\partial U_q}{\partial x_q} \tag{58}$$

It should be noticed that the angular momentum equation, e.g. equation 57, is decoupled with the linear momentum equation, e.g. equation 56, at the equilibrium state. At the same time, the linear momentum equation (equation 56) is identical to the classical Euler equation.

From these approximations to the balance laws, the material derivatives

found in equation 54 are obtained:

$$D(\rho) = v_l' \frac{\partial}{\partial x_l}\rho - \rho\frac{\partial U_q}{\partial x_q} \tag{59}$$

$$D(\theta) = v_l' \frac{\partial}{\partial x_l}\theta - \frac{1}{3}\theta\frac{\partial U_q}{\partial x_q} \tag{60}$$

$$D(U_i) = v_l' \frac{\partial}{\partial x_l}U_i - \frac{1}{\rho}\frac{\partial}{\partial x_i}(n\theta) \tag{61}$$

$$D(W_i) = v_l' \frac{\partial}{\partial x_l}W_i \tag{62}$$

With these final expressions substituted back into equation 54, the final form of g is given as:

$$\begin{aligned} g = -\tau f^{(0)}[&\frac{1}{\rho}(v_i'\frac{\partial \rho}{\partial x_i} - \rho\frac{\partial U_i}{\partial x_i}) \\ &- (\frac{3}{\theta} - \frac{m(v'^2 + j\omega'^2)}{2\theta^2})(v_i'\frac{\partial \theta}{\partial x_i} - \frac{\theta}{3}\frac{\partial U_q}{\partial x_q}) \\ &+ (\frac{mv_i'}{\theta})(v_l'\frac{\partial U_i}{\partial x_l} - \frac{1}{\rho}\frac{\partial}{\partial x_i}(n\theta)) \\ &+ (\frac{mj\omega_i'}{\theta})(v_l'\frac{\partial W_i}{\partial x_l})] \end{aligned} \tag{63}$$

Here, the first order distribution is now expressed entirely in terms of the mean and perturbed flow properties. All that remains is to find the first order approximations to the equations 34, 35, 36, and 37 to obtain non-zero expressions for the missing terms in the first-order balance laws 30, 31, 32, and 33.

For the first-order approximations to the above stresses, the definitions must now involve volume integrals of the first-order distribution function g:

$$q_\alpha^1 = \frac{m\rho}{2n}\int\int(v_l'v_l'v_\alpha' + \omega_p'\omega_p'v_\alpha')gd^3v'd^3\omega' \tag{64}$$

$$t_{\alpha\beta}^{\mathrm{Bol},1} = -\rho\int\int v_\alpha'v_\beta' g d^3v'd^3\omega' \tag{65}$$

$$t_{\alpha\beta}^{\mathrm{Cur},1} = -\rho\int\int \epsilon_{\beta pq}r_q\omega_p'v_\alpha' g d^3v'd^3\omega' \tag{66}$$

$$m_{\alpha\beta}^1 = -\frac{3\rho j}{2}\int\int \omega_\alpha'v_\beta' g d^3v'd^3\omega' \tag{67}$$

These volume integrals are more easily evaluated if they can be converted into

surface integrals. Applying albragic identities to the volume integrals yields:

$$
\begin{aligned}
q_\alpha^1 = &-\Bigg[\frac{8\pi^2 m\rho\tau}{3}\int\int dv'd\omega'(v'^6\omega'^2 + jv'^4\omega'^4) \\
&[-\frac{4}{\theta} + \frac{m(v'^2+j\omega'^2)}{2\theta^2}] \\
&(\frac{m\sqrt{j}}{2\pi\theta})^3 exp(-\frac{m(v'^2+j\omega'^2)}{2\theta})\Bigg]\frac{\partial\theta}{\partial x_\alpha} \\
&= -(4n\tau\theta)\frac{\partial\theta}{\partial x_\alpha}
\end{aligned}
\tag{68}
$$

$$
\begin{aligned}
t_{\alpha\beta}^{\mathrm{Bol},1} = &\Bigg[\frac{16\pi^2\tau\rho}{15\theta}\int v'^6\omega'^2(\frac{m\sqrt{j}}{2\pi\theta})^3 \\
&exp(-\frac{m(v'^2+j\omega'^2)}{2\theta})d\omega'dv'\Bigg] \\
&(\frac{\partial U_\alpha}{\partial x_\beta} + \frac{\partial U_\beta}{\partial x_\alpha} + \delta_{\alpha\beta}\frac{\partial U_l}{\partial x_l}) \\
&-\Bigg[\frac{16\pi^2\rho\tau}{3\theta}\int v'^4\omega'^2\frac{(v'^2+j\omega'^2)}{6}(\frac{m\sqrt{j}}{2\pi\theta})^3 \\
&exp(-\frac{m(v'^2+j\omega^2)}{2\theta})dv'd\omega'\Bigg]\delta_{\alpha\beta}\frac{\partial U_l}{\partial x_l} \\
&= n\tau\theta(\frac{\partial U_\alpha}{\partial x_\beta} + \frac{\partial U_\beta}{\partial x_\alpha}) - \frac{n\tau\theta}{3}(\frac{\partial U_l}{\partial x_l}\delta_{\alpha\beta})
\end{aligned}
\tag{69}
$$

$$
\begin{aligned}
t_{\alpha\beta}^{\mathrm{Cur},1} = &\Bigg[\frac{16\pi^2\rho\tau mj}{9\theta}(\frac{m\sqrt{j}}{2\pi\theta})^3\int v'^4\omega'^4 \\
&exp(-\frac{m(v'^2+j\omega'^2)}{2\theta})d\omega'dv'\Bigg]\epsilon_{\beta pq}r_q\frac{\partial W_p}{\partial x_\alpha} \\
&= (n\tau\theta)\epsilon_{\beta pq}r_q\frac{\partial W_p}{\partial x_\alpha}
\end{aligned}
\tag{70}
$$

$$
\begin{aligned}
m_{\alpha\beta}^1 = &\Bigg[\frac{48\pi^2\tau\rho j^2 m}{2\theta}\int \omega'^2v'^2\omega'_\beta v_\alpha\omega'_l v'_p(\frac{m\sqrt{j}}{2\pi\theta})^3 \\
&exp(-\frac{m(v'^2+j\omega'^2)}{2\theta})d\omega'dv'\Bigg]\frac{\partial W_l}{\partial x_p} \\
&= (\frac{3n\tau j\theta}{2})\frac{\partial W_\beta}{\partial x_\alpha}
\end{aligned}
\tag{71}
$$

The reduced forms of these stresses appear to follow familiar patterns. The heat flux in equation 68 appears to demonstrate a direct proportionality relationship with the temperature gradient. The Boltzmann stress contains terms related to the familiar strain-rates and divergences of the velocity. Still, these stresses all have nonlinear dependence on the temperature, meaning that simplifications will have to be made before direct comparisons with classical fluids can occur.

Equations 68, 69, 70 and 71 serve as the constitutive models for the first order approximation to the Boltzmann-Curtiss distribution and close the governing equations. A direct substitution of the stresses found in equations 68, 69, 70, and 71 into the first-order balance laws 38, 39, 40, and 41 yields

Continuity

$$\frac{\partial}{\partial t}\rho + \frac{\partial}{\partial x_l}(\rho U_l) = 0 \tag{72}$$

Linear Momentum

$$\begin{aligned}&\frac{\partial}{\partial t}(\rho U_s) + \frac{\partial}{\partial x_l}(\rho U_l U_s)\\ &- \frac{\partial}{\partial x_l}[-P\delta_{sl} + n\tau\theta(\frac{\partial U_l}{\partial x_s} + \frac{\partial U_s}{\partial x_l}) - \frac{n\tau\theta}{3}\frac{\partial U_q}{\partial x_q}\delta_{sl}] -\\ &\frac{\partial}{\partial x_l}(n\tau\theta\epsilon_{spq}r_q\frac{\partial W_p}{\partial x_l}) = 0\end{aligned} \tag{73}$$

Angular Momentum

$$\frac{\partial}{\partial t}(\rho j W_s) + \frac{\partial}{\partial x_l}(\rho j W_s U_l) - \frac{\partial}{\partial x_l}[(n\tau j\theta)\frac{\partial W_s}{\partial x_l}] = 0 \tag{74}$$

Energy

$$\frac{\partial}{\partial t}(\rho e) + \frac{\partial}{\partial x_l}(\rho e U_l) - \frac{\partial}{\partial x_l}(4n\tau\theta\frac{\partial \theta}{\partial x_l}) - \rho\langle v_l\frac{\partial e}{\partial x_l}\rangle = 0 \tag{75}$$

These equations contain derivatives of nonlinear terms and products of spatially varying variables. For this first-order approximation to the balance laws, the products of gradients of terms are presumed to vanish. Furthermore, equation 74 contains a spatial derivative of the spatial coordinate r_p that has its origin at the center of mass of the spherical particle. Looking at 1, the expression for this coordinate is easily derived in terms of the Eulerian coordinates: $r_i = x_i' - x_i$. Therefore, $\frac{\partial r_i}{\partial x_l} = -\delta_{il}$. Clearly the derivative is zero unless the components of x and r are the same. Taking this derivative into account, removing terms associated with products of gradients, and allowing for the existence of body forces, the governing equations become:

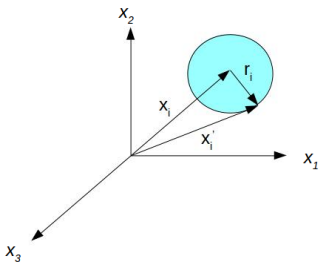

Figure 1: Illustration of the relationship between coordinates r_i and x_i

Continuity

$$\frac{\partial}{\partial t}\rho + \frac{\partial}{\partial x_l}(\rho U_l) = 0 \tag{76}$$

Linear Momentum

$$\frac{\partial}{\partial t}(\rho U_s) + \frac{\partial}{\partial x_l}(\rho U_s U_l) + \frac{\partial P}{\partial x_s} - n\tau\theta(\frac{\partial^2 U_s}{\partial x_l \partial x_l} + \frac{2}{3}\frac{\partial^2 U_l}{\partial x_l x_s}) - n\tau\theta\epsilon_{spq}\frac{\partial W_q}{\partial x_p} - \rho F_s = 0 \tag{77}$$

Angular Momentum

$$\frac{\partial}{\partial t}(\rho j W_s) + \frac{\partial}{\partial x_l}(\rho j W_s U_l) - n\tau j\theta\frac{\partial^2 W_s}{\partial x_l \partial x_l} - \rho L_s = 0 \tag{78}$$

Energy

$$\frac{\partial}{\partial t}(\rho e) + \frac{\partial}{\partial x_l}(\rho e U_l) - (4n\tau\theta)\frac{\partial^2 \theta}{\partial x_l \partial x_l} - \rho\langle v_l \frac{\partial e}{\partial x_l}\rangle - \rho H = 0 \tag{79}$$

In the preceding equations the body forces ρF_s and ρL_s have been introduced to account for external phenomena unrelated to the stresses previously introduced. Body forces for the linear momentum are easily found from the classical approach and require no special treatment. In the independent angular momentum equation, however, the factors affecting ρL_s are more subtle. 2 illustrates a body force created by the presence of vorticity near an individual particle. The connection between the two particles is symbolized by the coefficient ν_r. The motion of the right-hand particle creates the classical rotational motion, or macroscopic angular velocity, which induces the local rotation of the left particle. The amount of influence the angular velocity has on the gyration is determined by the value of ν_r. The body force disappears once the local rotation of the left particle equals the angular velocity, represented by half of the vorticity. De Groot and Mazur characterized this body force as an asymmetric pressure tensor [25], which had a linear relationship with the difference between the gyration and the angular velocity:

$$\rho L_s^{\text{interior}} = \nu_r(\epsilon_{spq}\frac{\partial U_q}{\partial x_p} - 2W_s) \tag{80}$$

Here, ν_r is designated as the "rotational viscosity," measuring the strength of induced gyration on a particle caused by the presence of a difference between its gyration and the local vorticity. This interior body force couples the local rotation with the translational velocity, ensuring that the linear momentum equation 77 and angular momentum equation 78 remain intertwined as long as the value of $\rho L_s^{\text{interior}}$ remains non-zero. The total angular momentum body force, ρL_s, can be viewed as the sum of this induced interior force and any external body moment force, $\rho L_s = \rho(L_s^{\text{interior}} + L_s^{\text{exterior}})$.

The continuity equation 76 is clearly the classical continuity equation for the mean velocity field. The deviation from classical kinetic theory becomes clear in the momenta equations. The compressible Navier-Stokes linear momentum equation, with the assumed satisfaction of Stokes's hypothesis, has the form:

$$\frac{\partial}{\partial t}(\rho U_s) + \frac{\partial}{\partial x_l}(\rho U_s U_l) + \frac{\partial P}{\partial x_s} - \mu\frac{\partial^2 U_s}{\partial x_l \partial x_l} - \frac{2\mu}{3}\frac{\partial^2 U_l}{\partial x_l \partial x_s} - \rho F_s = 0 \tag{81}$$

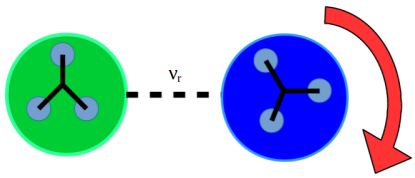

Figure 2: Diagram of the angular momentum body force L_s. Presence of vorticity induces gyration of left structure, with the strength of the coupling effect determined by ν_r.

Here, μ is the dynamic viscosity of the classical fluid. Comparing equations 81 and 77, the formulations are very similar, with the molecular viscosity from the Navier-Stokes equations represented by the expression $n\tau\theta$, as is expected from the first-order approximation to the Boltzmann transport equation [39]. The reduction of equations 76, 77, and 78 to the Navier-Stokes description will be discussed in more detail in the later part of the report.

The new term introduced by the preceding kinetic description has the form, $n\tau\theta\epsilon_{spq}\frac{\partial W_q}{\partial x_p}$. Here, the new variable of gyration, W_q, produces an additional source of linear momentum due to its transverse gradient. A notable insight is that the expression in front of the gyration gradient is also $n\tau\theta$, suggesting that the new term may contain a coefficient similar to the viscosity presented in classical fluids theory. To understand the meaning and importance of this new term in the linear momentum equation, the linear momentum equation from MCT is presented [86]:

$$\begin{aligned}\frac{\partial}{\partial t}(\rho U_s) + \frac{\partial}{\partial x_l}(\rho U_s U_l) + \frac{\partial P}{\partial x_s} \\ - (\lambda+\mu)\frac{\partial^2 U_l}{\partial x_l \partial x_s} - (\mu+\kappa)\frac{\partial^2 U_s}{\partial x_l \partial x_l} \\ - \kappa\epsilon_{spq}\frac{\partial W_q}{\partial x_p} - \rho F_s = 0\end{aligned} \tag{82}$$

Here, λ represents the second coefficient of viscosity and a new coupling coefficient, κ, is added to the total viscosity of the MCT fluid. Additionally, this coupling coefficient corresponds to the coefficient described in 2, as it determines the strength of the force induced by relative rotation within the MCT fluid. This theory, derived from the approach of rational continuum thermomechanics (RCT) [16, 26, 27, 28], starts with the same picture of the fluid and derives governing equations from kinematic and thermodynamic principles for a fluid with spherical particles. Comparing equations 77 and 82, the term associated with the transverse gradient in the kinetic equation now has a counterpart term associated with the coupling coefficient κ. Therefore, the first-order approximation to the Boltzmann-Curtiss transport equation produces a linear momentum equation consistent with the MCT formulation. Comparisons between the expressions for the coefficients in front of identical terms in these equations will shed light into the validity of these expressions for the new coefficients in MCT.

The simplification of the collisional term in equation 47 presumes that a singular relaxation time can be used to describe the transition from the real distribution function f to the equilibrium distribution function f^0. Due to the extra degrees of freedom introduced by the local rotation of the molecules, this relaxation time cannot be equated directly to the case of classical fluids. Still, as Chen et al demonstrated [13], expressions for a singular relaxation time can incorporate multiple processes or models involving several degrees of freedom. These expressions typically start from a base time constant applied to the relaxation of the motions of the molecular motion. In the current treatment, this base relaxation time would apply to the gyration.

De Groot and Mazur investigated the case of viscous flow in an isotropic fluid, but allowed for asymmetry in the pressure tensor. This asymmetry required for the consideration of an independent conservation theorem for angular momentum. Furthermore, pressure asymmetry generated "internal angular momentum," S_p, which arose from the local angular velocity, ω_p, of groups of particles at a point in the system. From conservation of angular momentum, De Groot and Mazur derived a balance equation for the internal angular momentum [25]:

$$\rho \frac{dS_q}{dt} = -2\Pi_q \tag{83}$$

Here, Π_q is the asymmetrical component of the pressure tensor. Internal angular momentum could be easily related to the angular velocity through $S_q = I\omega_q$, where I denoted the average moment of inertia of the constituent particles. The asymmetric pressure tensor, however, needed a more nuanced treatment. By deriving relations for the conservation of internal energy and entropy production, De Groot and Mazur found the thermodynamic force associated with the asymmetric pressure tensor [25]. This force emerged from a difference between the local and classical angular velocities, $\omega_s - \frac{1}{2}\epsilon_{spq}v_{q,p}$. Invoking Curie's principle [22] regarding thermodynamic fluxes and forces, De Groot and Mazur derived the following relation [25]:

$$\Pi_s = \nu_r(2\omega_s - \epsilon_{spq}\frac{\partial v_q}{\partial x_p}) \tag{84}$$

Clearly, the asymmetric pressure tensor mirrors the body force found in equation 80, indicating that the body force of the kinetic description can be obtained from a consideration of thermodynamic fluxes and forces. Given this closure relation, the conservation of internal angular momentum in equation 83 became:

$$\frac{d\omega_s}{dt} = -\frac{2\nu_r}{\rho I}(2\omega_s - \epsilon_{spq}\frac{\partial v_q}{\partial x_p}) \tag{85}$$

This equation is equivalent to the kinetic angular momentum equation 78 with the diffusion terms eliminated. Therefore, the kinetic theory is shown to obtain a more general form of a conservation equation. For the case of initially zero local angular velocity and constant vorticity, the solution to equation 85 becomes:

$$\omega_s = \frac{1}{2}\epsilon_{spq}\frac{\partial v_q}{\partial x_p}(1 - e^{-\frac{t}{\tau_o}}) \tag{86}$$

where the decay of the local angular velocity is characterized by a relaxation

time constant, τ_o, that has the form:

$$\tau_o = \frac{\rho I}{4\nu_r} \tag{87}$$

Measurements of diatomic hydrogen and deuterium mixtures at $p = 1$ atm and $T = 77K$ by Montero et al give a value of $2.20 \times 10^{-8} s$ for the rotational relaxation time [54]. Thus, the assumptions of zero initial local rotation, constant vorticity, and absence of external forces, leads to the derivation of a characteristic relaxation time that exclusively applied to internal angular momentum. These assumptions become relevant when the characteristic time is sufficiently reduced such that macroscale phenomena, such as the vorticity, can be approximated as constant compared with the evolution of local rotation. In these short time scales, equilibrium is achieved for the local rotation once it approaches the constant vorticity. Equation 87 provides a suitable first approximation of the characteristic relaxation time, τ, used in our kinetic theory description. De Groot's characterization of local angular velocity as the mean angular velocity of groups of particles matches the physical picture of our kinetic theory description. The addition of body forces into the governing kinetic theory equations can also incorporate the thermodynamic forces found in De Groot and Mazur's treatment. The rotational viscosity, ν_r, has a counterpart through the coupling coefficient κ in the MCT linear and angular momentum equations [15]. Therefore, numerical simulations of the kinetic and MCT descriptions should be able to determine the appropriate conditions for the use of equation 87 in this first order approximation.

The introduction of local rotation, ω_s, as an independent variable has resulted in a slightly different physical picture from the classical fluids description shown in the Navier-Stokes equations. The angular momentum equation 78 is not derived from the linear momentum equation 77, while the classical vorticity equation can only be derived from the classical linear momentum equation previously shown in equation 81. Still, the physical picture from which equations 76, 77, 78, and 79 are derived differs from Boltzmann's classical picture of a monatomic gas only through the introduction of the variable of gyration. When the gyration of a particle is distinct from macroscopic rotation, as defined by the angular velocity, $\frac{1}{2}\epsilon_{sab}\frac{\partial U_b}{\partial x_a}$, the new form of the linear momentum equation 77 and the independent angular momentum equation 78 can provide an alternative description to the classical Navier-Stokes picture. The difference of vorticity and gyration forms an objective (frame-indifferent) description of rotational motion, absolute rotation, as [15]

$$\Omega_s^{\mathrm{AR}} = \epsilon_{sab}\frac{\partial U_b}{\partial x_a} - 2W_s \tag{88}$$

The disappearance of absolute rotation indicates that vorticity is solely responsible for the local rotation and the dependence of gyration vanishes. Thus, such relation is called as angular equivalence. When zero absolute rotation occurs, i.e. angular equivalence, the gyration provides no new insight from the classical description. Therefore, the governing equations derived in previous sections should reduce to the Navier-Stokes equations. Setting $W_s = \frac{1}{2}\epsilon_{sab}\frac{\partial U_b}{\partial x_a}$ in the

governing momentum equations 77 and 78 yields:

Reduced Linear Momentum

$$\frac{\partial}{\partial t}(\rho U_s) + \frac{\partial}{\partial x_l}(\rho U_s U_l) + \frac{\partial P}{\partial x_s} - n\tau\theta(\frac{\partial^2 U_s}{\partial x_l \partial x_l} + \frac{2}{3}\frac{\partial^2 U_l}{\partial x_l \partial x_s}) - n\tau\theta\epsilon_{spq}\frac{\partial}{\partial x_p}(\frac{1}{2}\epsilon_{sab}\frac{\partial U_b}{\partial x_a}) - \rho F_s = 0 \tag{89}$$

Reduced Angular Momentum

$$\frac{\partial}{\partial t}(\rho\epsilon_{sab}\frac{\partial U_b}{\partial x_a}) + \frac{\partial}{\partial x_l}(\rho\epsilon_{sab}\frac{\partial U_b}{\partial x_a}U_l) - n\tau\theta\frac{\partial^2}{\partial x_l \partial x_l}(\epsilon_{sab}\frac{\partial U_b}{\partial x_a}) - 2\rho L_s^{\text{exterior}} = 0 \tag{90}$$

The common terms of the microinertia j and $\frac{1}{2}$ have been eliminated from equation 90. A key observation from equation 90 is the absence of the interior body force, $\rho L_s^{\text{interior}}$, described in equation 80. The difference in rotational motions necessary for the inducement of gyration on a particle has vanished, thus making $\rho L_s^{\text{interior}} = 0$. Meanwhile, equation 90 matches the form of the vorticity equation, derived from the curl of the Navier-Stokes linear momentum equation 81:

$$\frac{\partial}{\partial t}(\rho\epsilon_{sab}\frac{\partial U_b}{\partial x_a}) + \frac{\partial}{\partial x_l}(\rho\epsilon_{sab}\frac{\partial U_b}{\partial x_a}U_l) - \mu\frac{\partial^2}{\partial x_l \partial x_l}(\epsilon_{sab}\frac{\partial U_b}{\partial x_a}) - \rho\epsilon_{sab}\frac{\partial F_b}{\partial x_a} = 0 \tag{91}$$

Looking at the reduced linear momentum equation 89, further manipulations will show how this equation matches the classical picture. Using the identity for the Levi-Civita tensor $\epsilon_{sab}\epsilon_{spq} = \delta_{ap}\delta_{bq} - \delta_{aq}\delta_{bp}$ and contracting the appropriate indices, equation 89 becomes:

$$\frac{\partial}{\partial t}(\rho U_s) + \frac{\partial}{\partial x_l}(\rho U_s U_l) + \frac{\partial P}{\partial x_s} - n\tau\theta(\frac{\partial^2 U_s}{\partial x_l \partial x_l} + \frac{2}{3}\frac{\partial^2 U_l}{\partial x_l \partial x_s}) - \frac{n\tau\theta}{2}(\frac{\partial^2 U_p}{\partial x_s \partial x_p} - \frac{\partial^2 U_s}{\partial x_q \partial x_q}) - \rho F_s = 0 \tag{92}$$

Grouping together like terms yields the type II of the Navier-Stokes linear momentum equation:

$$\frac{\partial}{\partial t}(\rho U_s) + \frac{\partial}{\partial x_l}(\rho U_s U_l) + \frac{\partial P}{\partial x_s} - \frac{n\tau\theta}{2}\frac{\partial^2 U_s}{\partial x_l \partial x_l} - \frac{7n\tau\theta}{6}\frac{\partial^2 U_p}{\partial x_s \partial x_p} - \rho F_s = 0 \tag{93}$$

The form of the classical momenta equations is achieved when local rotation is indistinguishable from macroscopic rotation. Still, the precise formulation found in equations 93 and 90 requires a more detailed treatment. Following the classical kinetic theory formulation and Boltzmann distribution, it leads to the

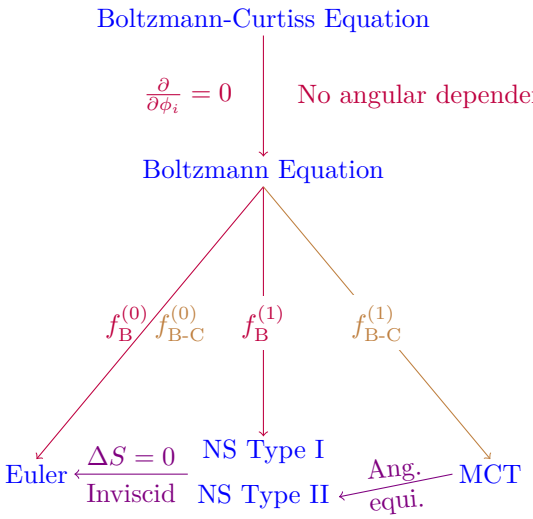

Figure 3: Pathway from morphing continuum theory to Navier-Stokes theory

Type I of the Navier-Stokes equations [39]:

$$\frac{\partial}{\partial t}(\rho U_s) + \frac{\partial}{\partial x_l}(\rho U_s U_l) + \frac{\partial P}{\partial x_s} - n\tau\theta \frac{\partial^2 U_s}{\partial x_l \partial x_l} - \frac{n\tau\theta}{3} \frac{\partial^2 U_p}{\partial x_s \partial x_p} - \rho F_s = 0 \tag{94}$$

In the type II of the Navier-Stokes equations, i.e. equation 93, the expression for the coefficient in front of the diffusion term is half that value in the Type I, i.e. equation 94, due to the contribution from the new term associated with the curl of the gyration. This term originally contained a coefficient that matched the form of the classical viscosity, but applied to the contribution of local rotation not found in the classical description. The temperature dependence of viscous rotational motion appears to have a slightly different limiting behavior as the particle rotation begins to resemble macroscopic motion.

Figure 3 shows the map between morphing continuum theory and Navier-Stokes equations from both the perspective of kinetic theory and rational continuum mechanics. From a kinetic point of view, Boltzmann equation can be obtained by dropping the angular dependence in the Boltzmann-Curtiss equation. For Boltzmann equations, two different distribution functions can be used to further deriving the conservation equations. The first one is the classical Boltzmann distribution. When the system is at the Boltzmann distribution (zero-th order approximation), i.e. equilibrium, the Boltzmann equation leads to Euler's equations. Furthermore, if the system is linearly deviated from the Boltzmann distribution (first order approximation), type I of the Navier-Stokes equation can be obtained. Similarly, if the Boltzmann -Curtiss distribution is adopted, the zero-th order approximation also leads to the Euler's equation. It is noticed that the first order approximation of the Boltzmann-Curtiss distribution is assumed for the system, the transport equation leads to morphing continuum theory as presented in this study. Interestingly, one of the correlations between

morphing continuum theory and the type II of the Navier-Stokes equations is the angular motion equivalence or the vanishing absolute rotation. As discussed in the previous section, the type I and II of Navier-Stokes equation differ in the angular motion dependence of the distribution functions. This concludes the theoretical development and relations between classical and morphing continua.

2.3 Objective Q-Criterion for Vortex&Eddy Visualization

Speziale devoted part of his career laying down the fundamentals of objectivity and investigated the requirement of objectivity over Galilean invariance for turbulence simulation [70, 71, 72, 73, 74]. More recently, Haller showed the inconsistency of vortex identification with the classical velocity gradient-based approaches and emphasized the importance of the objectivity or frame-indifference for vortex visualization [35]. The classical Q-criterion under NS framework relies on the second invariant of the velocity gradient, eg. $2II_a = v_{i,i}v_{j,j} - v_{i,j}v_{j,i} = \Omega_{ij}\Omega_{ji} - S_{ij}S_{ji}$; where $v_{i,j}$ is velocity gradient, $S_{ij} = \frac{1}{2}(v_{i,j} + v_{j,i})$ and $\Omega_{ij} = \frac{1}{2}(v_{i,j} - v_{j,i})$. It has been proven that the symmetric part of velocity gradient, S_{ij}, is objective; however the antisymmetric part , Ω_{ij} is only Galilean invariant.

The objectivity or frame-indifference emphasizes the invariance between two reference frames. Let a rectangular frame, M, be in relative rigid motion with respect to another one, M'. A point with rectangular coordinate x_k at time t in M will have another rectangular coordinate x'_k at time t' in M'. Since the reference frames are rigid motion with respect to each other, the motion between two frames can be described as $x'_k(t') = Q_{kl}(t)x_l(t) + b_k(t)$ where $Q_{kl}(t)$ is the rigid body rotation matrix between two frames and $b_k(t)$ is the translation between two frames. If the time derivative is performed on motion, it leads to $v'_k(t') = \dot{Q}_{kl}(t)x_l(t) + Q_{kl}(t)v_l(t) + \dot{b}_k(t)$. The velocity gradient between two frames can then be found as $v'_{k,m}(t') = \dot{Q}_{kl}(t)Q_{ml}(t) + Q_{kl}(t)Q_{mp}(t)v_{l,p}(t)$.

Therefore, the symmetric part of the velocity gradient between two frames is proven to be objective by $S'_{km} = \frac{1}{2}(v'_{k,m}(t')+v'_{m,k}(t')) = Q_{kl}(t)Q_{mp}(t)\frac{1}{2}(v_{l,p}(t)+v_{p,l}(t)) = Q_{kl}(t)Q_{mp}(t)S_{lp}$ where $\dot{Q}_{kl}(t)Q_{ml}(t) + \dot{Q}_{ml}(t)Q_{kl}(t) = \frac{d}{dt}Q_{ml}Q_{kl} = \frac{d}{dt}\delta_{km} = 0$.

Nevertheless, the antisymmetric part is found to be $\Omega'_{km} = \frac{1}{2}(v'_{k,m}(t') - v'_{m,k}(t')) = Q_{kl}(t)Q_{mp}(t)\Omega_{l,p} + \frac{1}{2}(\dot{Q}_{kl}(t)Q_{ml}(t) - \dot{Q}_{ml}(t)Q_{kl}(t))$. If the rotation matrix Q_{kl} is no longer time dependent, ie. $\dot{Q}_{kl}(t)Q_{ml}(t) = \dot{Q}_{ml}(t)Q_{kl}(t)) = 0$, Ω_{kl} is invariant. In other words, the antisymmetric part is Galilean invariant and only stays invariant between two frames with translation.

In MCT, the Cauchy stress is related to the velocity gradient and gyration through an objective strain-rate tensor, $a_{kl} = v_{l,k} + e_{lkm}\omega_m$ and $a'_{mn} = Q_{mk}Q_{nl}a_{kl}$. The objectivity of a_{kl} can be proven through a process similar to the aforementioned paragraph on velocity gradient. The orientation of inner structure is described by the director tensor, χ_{kK}. The director and its time derivative between two frames with rigid body motions can be shown as

$$\begin{aligned} &\chi'_{kK}(t') = Q_{km}(t)\chi_{mK}(t) \\ &\dot{\chi}'_{kK} = \dot{Q}_{km}\chi_{mK} + Q_{km}\dot{\chi}_{mK} \\ &e_{lkm}\omega'_m\chi'_{lK} = \dot{Q}_{km}\chi_{mK} + Q_{km}e_{amb}\omega_b\chi_{aK} \end{aligned} \tag{95}$$

where $\dot{\chi}_{mK} = e_{amb}\omega_b\chi_{aK}$, ω_b is the rotational velocity of an inner structure. After multiplying another director tensor on eq. 95, one can obtain $e_{mkp}\omega'_p = \dot{Q}_{kp}Q_{mp} + Q_{ma}Q_{kt}e_{atb}\omega_b$

From the previous paragraph, one can recall the velocity gradient described in two frames are related as $v'_{m,k} = \dot{Q}_{mp}Q_{kp} + Q_{ma}Q_{kt}v_{a,t}$ Therefore, one can see that

$$(v'_{m,k} + e_{mkp}\omega'_p) = Q_{ma}Q_{kt}(e_{etb}\omega_b + v_{a,t}). \tag{96}$$

Equation 96 proves the strain rate tensor, a_{km}, is objective.

As opposed to using the velocity gradient in NS equations for vortex identifications with Q-criterion, MCT relies on the strain rate tensors. The classical Q-criterion with the velocity gradient can be found as the second invariant of the velocity gradient, i.e. $Q = \frac{1}{2}(v_{i,i}v_{j,j} - v_{i,j}v_{j,i}) = \frac{1}{2}(\Omega_{ij}\Omega_{ji} - S_{ij}S_{ji})$, where S_{ij} is the symmetric part and Ω_{ij} is the antisymmetric part of the velocity gradient. Following a similar derivation, the MCT strain rate tensor can also be divided into a sum of a symmetric and antisymmetric part.

$$S^{\mathrm{MCT}}_{ij} = \frac{1}{2}(a_{ij} + a_{ji}) = \frac{1}{2}(v_{j,i} + v_{i,j}) \tag{97}$$

$$\Omega^{\mathrm{MCT}}_{ij} = \frac{1}{2}(a_{ij} - a_{ji}) = \frac{1}{2}(v_{j,i} - v_{i,j} + 2e_{jim}\omega_m) \tag{98}$$

It should be emphasized that since a_{ij} is objective, the addition or subtraction between objective tensors, e.g. S^{MCT}_{ij} and $\Omega^{\mathrm{MCT}}_{ij}$, remain objective. As a results, an objective Q-criterion for MCT is proposed as the second invariant of the strain rate tensor, a_{ij}, ie.

$$\begin{aligned} Q^{\mathrm{MCT}} &= \frac{1}{2}(a_{ii}a_{jj} - a_{ij}a_{ji}) \\ &= \frac{1}{2}(v_{i,i}v_{j,j} - v_{j,i}v_{i,j} - 2v_{j,i}e_{ijm}\omega_m + 2\omega_m\omega_m) \\ &= \frac{1}{2}(\Omega^{\mathrm{MCT}}_{ij}\Omega^{\mathrm{MCT}}_{ij} - S^{\mathrm{MCT}}_{ij}S^{\mathrm{MCT}}_{ij}) \end{aligned} \tag{99}$$

Using Cartesian Coordinate , the objective Q-criterion can be written as

$$\begin{aligned} Q^{\mathrm{MCT}} =& v_{x,x}v_{y,y} + v_{x,x}v_{z,z} + v_{y,y}v_{z,z} \\ &- (v_{x,y}v_{y,x} + v_{x,z}v_{z,x} + v_{y,z}v_{z,y}) \\ &- (v_{y,x} - v_{x,y})\omega_z - (v_{x,z} - v_{z,x})\omega_y \\ &- (v_{z,y} - v_{y,z})\omega_x + \omega_x^2 + \omega_y^2 + \omega_z^2 \end{aligned} \tag{100}$$

The symmetric part is the same as the one in NS theory showing the normal expansion of the flow behaviors. However, the physical meaning of the anti-symmetric part, $\Omega^{\mathrm{MCT}}_{ij}$, should be understood as absolute rotation. The off-diagonal part of an anti-symmetric matrix can be represented by a vector. Therefore, one can rewrite the antisymmetric part as a vector of absolute rotation (**A.R.**), i.e.$\mathbf{A.R.} = e_{ijk}\Omega^{\mathrm{MCT}}_{ij} = e_{ijk}v_{j,i} - 2\omega_k \sim \nabla \times \vec{v} - 2\vec{\omega}$

The first half of the **A.R.** is vorticity ($\nabla \times \vec{v}$) describing the relative rotation between two inner structure while the second half ($\vec{\omega}$) is the self-spinning of an inner structure. In other words, **A.R.** measures the phase shift or the rotational speed difference between the relative rotation and the self-spinning motion. This is the true rotation between two inner structures in a continuum

and it does not change even when observed from different reference frames. If **A.R.** is zero, it implies that the relative revolution between two inner structures is equal to the self-spinning motion. Therefore, two inner structures always face each other with the same side, like the Earth and the Moon. Without a global coordinate, the inner structure behaves as if there is no motion. Mathematically, **A.R.** = 0 reduces MCT back to NS equations [51]. This mathematical relation implies that if one believes vorticity can completely resolve all possible rotation without self-spinning gyration, NS theory and MCT are equivalent. It is noted that Truesdell followed the monumental work by Grad [32] and derived a balance law of internal rotation [80, 82]. De Groot and Mazur also discussed a similar governing equation in their book [25]. The concept of the internal rotation is similar to the new degrees of freedom, gyration, in MCT. However, De Groot and Mazur derived the balance law from a mechanics perspective so the time evolution of the intrinsic rotation is only governed by the antisymmetric part of Cauchy stress, i.e. $e_{kij}t_{ij}$. On the other hand, the constitutive equation of gyration in MCT was derived from the classical nonequilibrium thermodynamics. Therefore, there is an additional moment stress, i.e. $m_{lk,l}$. Consequently, there is a dissipation or diffusion mechanism in the balance law of angular momentum, i.e. $\omega_{k,ll}$. The diffusion of gyration leads to the heat and eventually the irreversible entropy generation.

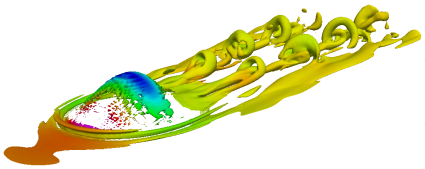

Figure 4: Hairpin eddy structure identified by the objective Q-Criterion with MCT

Figure 4 shows the iso-surface of the objective Q-Criterion for the coherent eddy structure in the transonic flow over a three-dimensional bump. The iso-surface is colored by the magnitude of the absolute rotation (**A.R.**). The hairpin structure of the eddies are clearly seen without being limited by the Galilean invariance.

3 Numerical Validation of MCT and Applications

The team has also developed a finite volume-based numerical solver for compressible flows with shock preservation. The accuracy of the numerical solver has been proven to be second order in space and time [12]. The numerical solution was compared with the test case of 2-D compression ramp (experiments done by Kuntz [48]) for validation. The details of validation is published in Physical Review Fluids [12].

3.1 Numerical Scheme for Morphing Continuum

The team has presented a second-order shock-preserving scheme for morphing continuum. The following part shows the scheme is second order accurate and

has been used in several of the PI's publications. These publications include a study in supersonic turbulence published in *Physical Review Fluids* [12], one in transonic turbulence in *AIAA Journal* [84] and hypersonic flows in AIAA and APS conferences [2].

The presented numerical scheme has also been shown computationally effective. The numerical solver has been implemented in the structure for parallel computing. Beyond the numerical and computational optimization, the multiscale nature of MCT also shows the computational advantage in direct numerical simulation (DNS) over the classical Navier-Stokes equations. For the supersonic turbulence study in *Physical Review Fluids* [12], the grid spacing near the wall in the MCT study is $\Delta y^+ = 1.34$ with 10 grid points for $y^+ < 30$, while for a similar DNS simulation [87], the required spacing normal to the wall is $\Delta y^+ = 0.2$ with more than 20 grid points in $y^+ < 20$. Also, for the transonic turbulence study in *AIAA Journal* [84], the total number of grid points is about 6 million while the comparative NS study requires 54 M grid points [11]. Unlike the classical DNS replying on fine meshes to resolve subscale motions, MCT formulates subscale motions into the governing equations. therefore, the mesh requirements for MCT are less restrictive than DNS, resulting in MCT being a more computationally-friendly theory.

The MCT governing equations for a compressible flow can be found:
Conservation of Mass:

$$\frac{D\rho}{Dt} + \rho v_{m,m} = 0 \tag{101}$$

Conservation of Linear Momentum:

$$\begin{aligned} \rho \frac{Dv_m}{Dt} = -p_{,m} + (\lambda + \mu) v_{n,nm} + (\mu + \kappa) v_{m,nn} \\ + \kappa(\epsilon_{mnk}\omega_{k,n}) \end{aligned} \tag{102}$$

Conservation of Angular Momentum:

$$\begin{aligned} \rho j \frac{D\omega_m}{Dt} = (\alpha + \beta)\omega_{n,nm} + \gamma \omega_{m,nn} \\ + \kappa(\epsilon_{mnk} v_{k,n} - 2\omega_m) \end{aligned} \tag{103}$$

Conservation of Energy:

$$\begin{aligned} \rho \frac{DE}{Dt} = &-(pv_m)_{,m} + (\lambda v_{m,m} v_k)_{,k} + [\kappa(v_{l,k} v_l \\ &+ \epsilon_{kml}\omega_m v_l) + \mu(v_{l,k} + v_{k,l}) v_l]_{,k} \\ &+ (\alpha \omega_{m,m}\omega_k + \beta \omega_{k,l}\omega_l + \gamma \omega_l \omega_{l,k})_{,k} \\ &+ (KT_{,k})_{,k} \end{aligned} \tag{104}$$

where $E = e + 1/2(v_m v_m + j\omega_m \omega_m)$ is the total energy density of the fluid , and e is the internal energy. α_T disappears after substitution into the balance laws, since $m_{kl,k}$ and $q_{k,k}$ will yield $\frac{\alpha_T}{T} e_{klm} T_{,mk} = 0$ and $\frac{\alpha_T}{T} e_{klm}\omega_{m,lk} = 0$ .To close this system of equations the fluid is assumed to be an ideal gas, leading to the

following relations:

$$e = c_v T = c_v \frac{p}{\rho(c_p - c_v)} \tag{105}$$

$$\rho E = \frac{p}{\frac{c_p}{c_v} - 1} + \frac{1}{2}\rho(v_m v_m + j\omega_m \omega_m) \tag{106}$$

where c_p is the specific heat at constant pressure and c_v is the specific heat at constant volume.

To better understand the contribution of the individual eddies, the MCT governing equations be non-dimensionalized, where the dimensionless groups are defined based on the physical parameters of interest. Starting with the distance and motion variables, the length scales x_m, and the translation velocity v_m will be parameterised with the square-root of the subscale inertia $L = \sqrt{j}$, and the freestream velocity U_∞ respectively. The temporal term t will be dimensionalized with the time it takes the freestream velocity to cover the distance L, i.e. L/U_∞. The gyration, ω_m, meanwhile, will be dimensionalized with the inverse of temporal term. In summary the dimesionless variables are:

$$\begin{aligned} \hat{x}_m &= \frac{x_m}{L} \quad \hat{v}_m = \frac{v_m}{U_\infty} \\ \hat{t} &= \frac{t}{L/U_\infty} \quad \hat{w}_m = \frac{w_m}{U_\infty/L} \end{aligned} \tag{107}$$

The thermodynamic variables of the density, ρ, and pressure, p, will be dimensionalized according to the freestream density ρ_∞ and dynamic pressure ρU_∞^2. Substituting the nondimensionalized variables into the governing equations yields a set of dimensionless groups that captures the physical behavior of each parameter. One parameter is the Reynolds number, which is defined as the ratio of the convection to the diffusion of linear momentum,

$$Re = \frac{\rho_\infty U_\infty L}{\mu + \kappa} \tag{108}$$

As for the energy equation two dimensionless numbers appear; the Prandtl number, which defines the ratio of momentum diffusivity to thermal diffusivity, and the Eckert number, which defines the relationship between a flow's kinetic energy and the boundary layer enthalpy difference,

$$Pr = \frac{c_p(\mu + \kappa)}{K} \qquad Ec = \frac{U_\infty^2}{c_p T_\infty} \tag{109}$$

The previously defined parameters are typical dimensionless groups found in the classical fluid theory. The next dimensionless term that is specific to MCT, will be called Er in honor of Eringen and is defined as the ratio of the inertial forces to the viscous forces arising from the gyration,

$$Er = \frac{\rho_\infty U_\infty L}{\kappa} \tag{110}$$

The other parameters found in MCT will also be non-dimensionlised with respect to the convection term

$$C_\alpha = \frac{\rho_0 U_\infty L^3}{\alpha} \quad C_\beta = \frac{\rho_0 U_\infty L^3}{\beta} \quad C_\gamma = \frac{\rho_0 U_\infty L^3}{\gamma} \tag{111}$$

In this regard the governing equations in dimensionless form become:

Conservation of Mass:

$$\frac{\partial \hat{\rho}}{\partial \hat{t}} + \hat{\nabla}\left(\hat{\rho}\hat{\mathbf{v}}\right) = 0 \tag{112}$$

Conservation of Linear Momentum:

$$\begin{aligned}\frac{\partial(\hat{\rho}\hat{\mathbf{v}})}{\partial \hat{t}} + \hat{\nabla}\left(\hat{\mathbf{v}}(\hat{\rho}\hat{\mathbf{v}})\right) = -\hat{\nabla}\hat{p} + \frac{1}{Re}\left[\frac{1}{3}\hat{\nabla}(\hat{\nabla}\hat{\mathbf{v}})\right. \\ \left.+\hat{\nabla}^2\hat{\mathbf{v}}\right] + \frac{1}{Er}\left[\hat{\nabla}\times\hat{\boldsymbol{\omega}} - \frac{2}{3}\hat{\nabla}(\hat{\nabla}\hat{\mathbf{v}})\right]\end{aligned} \tag{113}$$

Conservation of Angular Momentum:

$$\begin{aligned}\frac{\partial(\hat{\rho}\hat{\boldsymbol{\omega}})}{\partial \hat{t}} + \hat{\nabla}\left(\rho\hat{\mathbf{v}}\hat{\boldsymbol{\omega}}\right) = \left(\frac{1}{C_\alpha} + \frac{1}{C_\beta}\right)\hat{\nabla}(\hat{\nabla}\hat{\boldsymbol{\omega}}) \\ + \frac{1}{C_\gamma}\hat{\nabla}^2\hat{\boldsymbol{\omega}} + \frac{1}{Er}\left(\hat{\nabla}\times\hat{\mathbf{v}} - 2\hat{\boldsymbol{\omega}}\right)\end{aligned} \tag{114}$$

Conservation of Energy:

$$\begin{aligned}\frac{\partial\hat{\rho}\hat{E}}{\partial\hat{t}} + \hat{\nabla}(\hat{\rho}\hat{E}\hat{\mathbf{v}}) = -\hat{\nabla}(\hat{p}\hat{\mathbf{v}}) + \frac{1}{Re}\hat{\nabla}\left[[\hat{\nabla}\hat{\mathbf{v}}]^T\hat{\mathbf{v}}\right. \\ \left.+\hat{\mathbf{v}}\hat{\nabla}\hat{\mathbf{v}} - \frac{2}{3}\hat{\mathbf{v}}(\hat{\nabla}\hat{\mathbf{v}})\right] + \frac{1}{Er}\hat{\nabla}\left[\frac{1}{3}\hat{\mathbf{v}}(\hat{\nabla}\hat{\mathbf{v}})\right. \\ \left.+\hat{\boldsymbol{\omega}}\times\hat{\mathbf{v}} - [\hat{\nabla}\hat{\mathbf{v}}]^T\hat{\mathbf{v}}\right] + \frac{1}{C_\alpha}\hat{\nabla}((\hat{\nabla}\hat{\boldsymbol{\omega}})\hat{\boldsymbol{\omega}}) \\ + \frac{1}{C_\beta}\hat{\nabla}((\hat{\nabla}\hat{\boldsymbol{\omega}})\hat{\boldsymbol{\omega}}) + \frac{1}{C_\gamma}\hat{\nabla}\left(\hat{\boldsymbol{\omega}}(\hat{\nabla}\hat{\boldsymbol{\omega}})^T\right) \\ + \frac{1}{ReEcPr}\hat{\nabla}^2\hat{T}\end{aligned} \tag{115}$$

The solver developed to implement the MCT compressible governing equations is be constructed in the framework of the finite volume discretization. One reason for choosing finite volume is due to its easy implementation, and its convergence to a stable solution for complex flows. The spatial domain implemented is divided into contiguous control volumes or cells, with the physical variables of velocity, gyration, pressure, density and temperature collocated (i.e. located at the cell center).
The transport equation for any conserved property can be written in following form,

$$\underbrace{\frac{\partial\phi}{\partial t}}_{\text{transient term}} + \underbrace{\nabla(\mathbf{v}\phi)}_{\text{convective term}} = \underbrace{\nabla(\Gamma_\phi\nabla\phi)}_{\text{diffusive term}} + \underbrace{S_\phi}_{\text{source term}} \tag{116}$$

Here, ϕ refers to a transport variable, Γ_ϕ is the diffusivity or the diffusion coefficient, and S_ϕ is the source term. Letting $\phi = \rho$ yields the continuity equation, $\phi = \rho v_m$ gives the linear momentum equation, $\phi = j\rho\omega_m$ yields the angular momentum equation and $\phi = \rho E$ gives the energy equation. The finite volume method requires that the governing equations in their integral form be

satisfied over the control volume. Applying spatial integration on equation 116,

$$\int_{V_c} \frac{\partial \phi}{\partial t} dV + \int_{V_c} \nabla(\mathbf{v}\phi) dV = \int_{V_c} \nabla(\Gamma_\phi \nabla \phi) dV \int_{V_c} S_\phi dV \tag{117}$$

For the present solver, a simple forward Euler was implemented for the unsteady term,

$$\int_{V_c} \frac{\partial \phi}{\partial t} dV = \frac{\phi_c^{n+1} - \phi_c^n}{\triangle t} V_c \tag{118}$$

where V_c represents the cell volume, the subscript c refers to the cell center, and superscript n refers to the current time step. Implementing forward Euler on the conservation of mass, linear momentum, angular momentum, and energy equations yields:

$$\int_{V_c} \frac{\partial \hat{\rho}}{\partial \hat{t}} dV \approx \frac{\hat{\rho}_c^{n+1} - \hat{\rho}_c^n}{\triangle \hat{t}} V_c \tag{119}$$

$$\int_{V_c} \frac{\partial (\hat{\rho}\hat{\mathbf{v}})}{\partial \hat{t}} dV \approx \frac{(\hat{\rho}\hat{\mathbf{v}})_c^{n+1} - (\hat{\rho}\hat{\mathbf{v}})_c^n}{\triangle \hat{t}} V_c \tag{120}$$

$$\int_{V_c} \frac{\partial (\hat{\rho}\hat{\boldsymbol{\omega}})}{\partial \hat{t}} dV \approx \frac{(\hat{\rho}\hat{\boldsymbol{\omega}})_c^{n+1} - (\hat{\rho}\hat{\boldsymbol{\omega}})_c^n}{\triangle \hat{t}} V_c \tag{121}$$

$$\int_{V_c} \frac{\partial (\hat{\rho}\hat{E})}{\partial \hat{t}} dV \approx \frac{(\hat{\rho}\hat{E})_c^{n+1} - (\hat{\rho}\hat{E})_c^n}{\triangle \hat{t}} V_c \tag{122}$$

This scheme is first order in time, but can be modified to a higher-order Runge-Kutta time integration scheme.

Critical care is considered for the numerical scheme implemented on the convection terms in MCT, which are $\hat{\nabla}(\hat{\rho}\hat{\mathbf{v}})$,$\hat{\nabla}(\rho\hat{\mathbf{v}}\hat{\mathbf{v}})$, $\hat{\nabla}(\rho\hat{\mathbf{v}}\hat{\boldsymbol{\omega}})$, and $\hat{\nabla}(\hat{\rho}\hat{E}\hat{\mathbf{v}})$. The numerical scheme adopted for the convection terms should be able to capture the shock wave and discontinuities, while avoiding oscillations. Replacing the volume integral by a surface integral through the use of the divergence theorem, the convection terms can be approximated as,

$$\int_{V_c} \nabla(\mathbf{v}\phi) dV = \oint_S (\mathbf{v}\phi) d\mathbf{S} \approx \sum_f \mathbf{v}_f \phi_f \mathbf{S}_f \tag{123}$$

where $\sum_f$ denotes the summation over the faces of the control volume, $\mathbf{v}_f \mathbf{S}_f$ is the volumetric flux, $\mathbf{S}_f$ is the face normal vector, and ϕ_f represents the face value of the transport variable. Notable methods found in the literature are able to effectively produce accurate non-oscillatory solutions for ϕ_f. These methods are: piecewise parabolic method (PPM) [21]; essentially non-oscillatory (ENO) [66, 37]; weighted ENO (WENO) [50]; and the Runge-Kutta discontinuous Galerkin (RKDG) method [20]. All of these methods involve Riemann solvers, characteristic decomposition and Jacobian evaluation, making them troublesome to implement. The scheme implemented in this study is a second-order semi-discrete, non-staggered scheme, introduced by Kurganov, Noelle and Petrova (KNP) [49] as a second-order generalized Lax-Friedrichs scheme. The interpolation procedure of the transport variable ϕ from the cell center, ϕ_c, to the face center, ϕ_f, implemented in this scheme is split into two

directions corresponding to the outward or inward direction of the face normal,

$$\sum_f \mathbf{v}_f \phi_f \mathbf{S}_f = \sum_f [\boldsymbol{\alpha} \mathbf{S}_{f+} \mathbf{v}_{f+} \phi_{f+} + (1-\boldsymbol{\alpha}) \mathbf{S}_{f-} \mathbf{v}_{f-} \phi_{f-} + \boldsymbol{\omega}_f (\phi_{f-} + \phi_{f+})] \tag{124}$$

where $\mathbf{S}_{f+}$ is the same as $\mathbf{S}_f$ and $\mathbf{S}_{f-} = -\mathbf{S}_f$. The subscript $f+$ is denoted for the directions coinciding with $\mathbf{S}_{f+}$, and $f-$ for the opposite direction. The two terms $\mathbf{S}_{f+}\mathbf{v}_{f+}\phi_{f+}$ and $\mathbf{S}_{f-}\mathbf{v}_{f-}\phi_{f-}$ in equation 124 represent the fluxes evaluated at the $\mathbf{S}_{f+}$ and $\mathbf{S}_{f-}$ directions respectively. The last part of equation 124 represents an additional diffusive term based on the maximum speed of propagation of any discontinuity that may exist at the face. The weighted coefficient $\boldsymbol{\alpha}$ is,

$$\boldsymbol{\alpha} = \frac{\psi_{f+}}{\psi_{f+} + \psi_{f-}} \tag{125}$$

where $\psi_{f\pm}$ is the local speed of propagation, shown to be:

$$\psi_{f+} = max\left(c_{f+}|\mathbf{S}_f| + \phi_{f+}, c_{f-}|\mathbf{S}_f| + \phi_{f-}, 0\right) \tag{126}$$

$$\psi_{f-} = max\left(c_{f+}|\mathbf{S}_f| - \phi_{f+}, c_{f-}|\mathbf{S}_f| - \phi_{f-}, 0\right) \tag{127}$$

and $c_{f\pm} = \sqrt{\gamma R T_{f\pm}}$ is the local speed of sound at the face. The diffusive volumetric flux $\boldsymbol{\omega}_f$, has the form,

$$\boldsymbol{\omega}_f = \boldsymbol{\alpha}(1-\boldsymbol{\alpha})(\psi_{f+} + \psi_{f-}) \tag{128}$$

The scheme implemented to interpolate the values at the center of the face in the directions of $\mathbf{S}_{f+}$ and $\mathbf{S}_{f-}$ is based on the limiting standard first and second order upwind [31]. The interpolation at $f+$ for example is,

$$\phi_{f+} = (1 - g_{f+})\phi_O + g_{f+}\phi_N \tag{129}$$

where the subscripts O and N represent the nodes at the center of the owner cells and neighbor cells respectively, and the KNP geometric weighting factor $g_{f+} = \beta_f(1 - w_f)$ with β_f being the van-Leer limiter function.

All of the gradient terms in the MCT governing equations are computed using the Green-Gauss theorem [58, 55],

$$\int_{V_c} (\nabla\phi)_c dV = \sum_f \phi_f \mathbf{S}_f \tag{130}$$

where the face value is calculated using the compact stencil method [55], which is simply the geometric average of the two cell-centered values of the face,

$$\phi_f = g_c\phi_O + (1 - g_c)\phi_N \tag{131}$$

where g_c is the geometric weighting factor. The only exception is the pressure gradient, $\hat{\nabla}p$, in the linear momentum equation which was discretized according to the Kurganov, Noelle and Petrova (KNP) [49] flux splitting scheme,

$$\sum_f \phi_f \mathbf{S}_f = \sum_f [\boldsymbol{\alpha} \mathbf{S}_{f+} \phi_{f+} + (1-\boldsymbol{\alpha}) \mathbf{S}_{f-} \phi_{f-}] \tag{132}$$

where α is the weighted cofficient defined previously.

H

Table 1: Algorithm for Solving the MCT governing equations

while t < End Time:
Interpolate all the fields from the cell center to face center
Calculate the convective, diffusive, and gradient terms
Solve the continuity equation for ρ
Solve the linear momentum equation for u_i
Solve the angular momentum equation for ω_i
Solve the energy equation for E
Update the temperature T from E
Update the pressure using the ideal gas law
Update the boundary conditions
Update time ($t^{n+1} = t^n + \Delta t$)

Finally, the diffusion terms are approximated by,

$$\int_V \nabla(\Gamma_\phi \nabla\phi) dV = \int_S (\Gamma_\phi \nabla\phi) d\mathbf{S} \approx \sum_f (\Gamma_\phi \nabla\phi)_f . \mathbf{S}_f \tag{133}$$

The $(\Gamma_\phi \nabla\phi)_f$ term can be obtained as the weighted average of the gradients at the face centroids multiplied by the diffusivity at the centroid,

$$(\Gamma_\phi \nabla\phi)_f = g_c(\Gamma_\phi \nabla\phi)_O + (1 - g_c)(\Gamma_\phi \nabla\phi)_N \tag{134}$$

In most cases, the diffusivity is interpolated linearly from the cell center values to the faces. The curls of the transport variables are represented by the off diagonal components in the antisymmetric part of the corresponding Green-Gauss gradients. Therefore, the curls of these variables can be computed in a similar fashion to the gradient terms.

Now that the specifics of the finite volume solver have been described, the final step is to give an overview of the algorithm employed. The solver developed is a fully explicit solver: all terms in the MCT governing equations are evaluated at the previous time step. This approach enables fewer computations per time step, but does put a constraint on the size of the time step. The full algorithm of the MCT solver is shown in table 1. With this algorithm in place, numerical simulation of the compressible flow can be done through the perspective of MCT.

Verification of the compressible MCT solver was done by comparing the numerical results of the compressible isothermal Couette flow with the analytical solution. The assumptions for the Couette flow are that the flow is fully developed, steady state, isothermal, incompressible, and two-dimensional [17], i.e. zero velocity in the y and z direction and zero gyration in the x and y direction.

Under these assumptions the governing equations for MCT are reduced to:

$$(\mu + \kappa)\frac{\partial^2 v_x}{\partial y^2} + \kappa\frac{\partial \omega_z}{\partial y} = 0 \tag{135}$$

$$\gamma\frac{\partial^2 \omega_z}{\partial y^2} - \kappa\frac{\partial v_x}{\partial y} - 2\kappa\omega_z = 0 \tag{136}$$

As for the boundary conditions, the moving plate is placed at a height h above

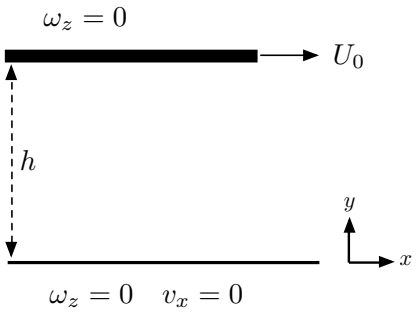

Figure 5: Boundary conditions for a 2D Couette Flow

the fixed plate, and moves in the x-direction at the a velocity U_0, while the gyration at both plates is fixed at zero due to the no-slip condition. Figure 5 illustrates the boundary conditions of the system. The analytical solutions of gyration and velocity for the Couette flow are,

$$\omega_z = C_1 S \left[-1 + \left(1 - \frac{1}{D}\right) e^{-My} + \frac{e^{My}}{D} \right] \tag{137}$$

$$v_x = C_4 + C_1 \left[y + \frac{GS}{M} \left(-\left(1 - \frac{1}{D}\right) e^{-My} + \frac{e^{My}}{D} - My \right) \right] \tag{138}$$

where:

$$M = \sqrt{\frac{\kappa(2\mu + \kappa)}{\gamma(\mu + \kappa)}}; \quad D = 1 + e^{Mh}; \quad S = \frac{\kappa + \mu}{\kappa + 2\mu}$$

$$G = -\frac{\kappa}{\kappa + \mu}; \quad C_4 = \frac{(-2 + D)e^{hM} SG}{F} U_0;$$

$$C_1 = \frac{D e^{hM} M}{F} U_0;$$

$$F = \left(-1 + e^{hM}\right)^2 GS + D\left[-GS + e^{hM}(hM + GS - GhMS)\right]$$

The details of the numerical order calculation and verification for the velocity and gyration are shown in Table 2 and Table 3. The results clearly indicate that the solver exhibits the desired optimal second order of accuracy.

3.2 Validation1 : Supersonic Compression Ramp

Kuntz et. al.'s experiment [47, 48] of a supersonic flow over an 8° compression ramp is replicated. In his paper Kuntz et. al. considered a series of five compression ramps ranging from 8° to 24°. Using this set of ramp angles Kuntz was able to capture a full range of possible flow fields, including flow with no separation, flow with incipient separation, and flow with a sig-

Table 2: Velocity error analysis

	Vel L_1	Order	Vel L_2	Order	Δx_m
5x5	0.026486	1.613	0.019180	1.681	0.2
10x10	0.008657	1.569	0.005981	1.717	0.1
20x20	0.002918	1.334	0.001818	1.632	0.05
40x40	0.001157	-	0.000586	-	0.025

Table 3: Gyration error analysis

	Gyr L_1	Order	Gyr L_2	Order	Δx_m
5x5	0.076868	1.408	0.026486	1.579	0.2
10x10	0.028963	1.672	0.008657	1.769	0.1
20x20	0.009088	1.456	0.002918	1.693	0.05
40x40	0.003312	-	0.001157	-	0.025

nificant amount of separation. Kuntz et. al.'s experimental data has been referenced to derive shock-wave/boundary-layer interaction (SWBLI) models based on mass conservation [68]. In addition, this data was used to validate the accuracy of different RANS models [56, 5], to analyze the significance of the spanwise geometry variation and to relate it to a canonical compression flow for a three-dimensional bump flowfield [79]. For the 8° compression ramp, Kuntz's experimental results showed no separation of the flow near the corner ramp, making it an ideal simple case to demonstrate the capabilities of MCT. Another reason why the 8° compression ramp is chosen is the two-dimensional behavior of the shock near the ramp corner, giving credence to the assumption of a two-dimensional flow, as well as the adiabatic condition at the wall, resulting in no heat dissipation. Figure 6 shows a schematic for the present ramp configuration.

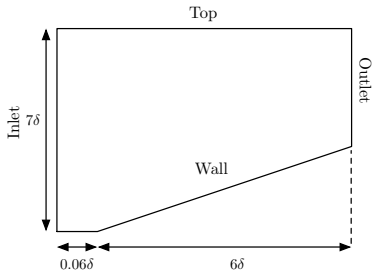

Figure 6: Size of the compression ramp computational domain

The working fluid is assumed to be an ideal gas, where the equation of state is $p = \rho RT$. The gas constant is taken as $R = 287.06\ m^2 s^{-2} K^{-1}$, the specific heat coefficient for constant pressure is $c_p = 1004.06\ J/(kgK)$ and the Prandtl number is $Pr = 0.7$. The summation of all the viscous coefficients were computed by Sutherland's law, $\kappa + \mu = \frac{(1.458\times10^{-6})T^{3/2}}{T+110.4}$.

The temperature at the wall was set to adiabatic conditions, in reference to the experiments by Kuntz et. al. [47]. The boundary layer thickness, δ, and the momentum layer thickness, θ, for the incoming flow, reported by Kuntz et. al. [47], at the location of the ramp edge were measured to be 8.27 mm and 0.57 mm. As for the MCT variables, Wonnell and Chen [86] showed that the viscous forces arising from the gyration should be around 99 times the dynamic viscosity (i.e. $\kappa = 99\mu$) to obtain a turbulent incompressible

flow. This study follows the work of Wonnell and Chen by making κ equal to 99μ [86]. The two other dimensionless parameters (C_α and C_β) are set to zero, since currently there is no physical meaning to them.

The subject of spatially evolving turbulent flows poses a particular challenge for numerical simulation, due to the need for time-dependent inlet conditions at the upstream boundary. In many cases, the downstream flow is highly dependent on the conditions of the inlet. Therefore it is necessary to specify a realistic time series of turbulent fluctuations that are in equilibrium with the mean flow, while still satisfying the governing equations. For this reason, creating accurate inflow turbulent conditions may require costly independent simulations [52], forced transition [61], a long leading edge [56], or cost-saving but crude inflow generation methods [88].

Oliver tested turbulent RANS models for a flow past an 8° compression ramp [56]. In this study, the length of the flat plate upstream of the ramp corner exceeded 60δ. The reason for this addition was to allow the inflow to develop from a uniform to a turbulent flow, with a boundary layer that matched the experimental boundary layer thickness.

Here, MCT has the ability to control the eddy structure of the flow by the gyration term, enabling it to model turbulence without the need for complex boundary conditions. Wonnell and Chen [86] showed through utilizing the subscale eddies near the wall that MCT can control the regime of the flow and change it from laminar to transitional or turbulent. They later showed that in addition to controlling the eddies near the wall, one can control the eddies' rotational speed at the inlet, and thus control the incoming turbulent kinetic energy $1/2\rho j\omega_k\omega_k$ [85].

The inflow variables implemented in the current case to achieve a turbulent flow are decomposed into two parts, the mean and fluctuating components. For the mean flow, a prescribed turbulent mean velocity profile was defined at the inlet, through the implementation of Martin's procedure [52].

The fluctuations are generated by controlling the rotational speed of the upstream eddies. This happens because the instantaneous inlet gyration ω_k is decomposed into mean and fluctuating parts, $\omega_k(t,y) = \langle\omega_k(y)\rangle + \omega'_k(t,y)$ where $\langle\omega_k\rangle$ is the mean value of the gyration, and $\omega'_k(t)$ is the fluctuating rotation speed of the eddy. The perturbations are produced through a random number generator with the range of values constrained by the root-mean squared (rms) gyration, and turbulent intensity from the experiments at the specified point. The rms value of the perturbed gyration becomes $\omega_{rms} = \sqrt{\frac{1}{N}\sum_{k=1}^{N}\omega'_i\omega'_i}$ and the turbulent intensity of the MCT flow becomes $I = \frac{\omega_{rms}d/2}{U_\infty}$ It can be seen that the larger the range of the perturbation in the gyration field the larger the rms value and thus the larger the turbulent intensity. In order to focus on the effects of the fluctuations, the mean gyration was set to zero, while the amplitude of the perturbed gyration was

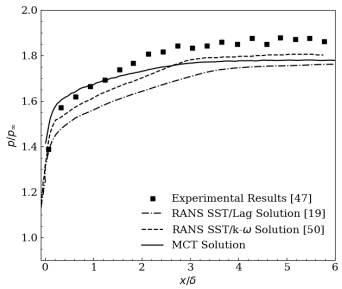

Figure 7: Mean wall pressure distribution from MCT and experimental results

defined so that the turbulent intensity of the incoming flow matches the experimental turbulent intensity results of Kuntz et. al.

The boundary conditions of pressure and temperature at the inlet are set to the freestream conditions. At the outlet and top boundaries, supersonic outflow boundary conditions are implemented, and for the ramp wall the no-slip and adiabatic boundary conditions are implemented.

A structured grid is generated, with the distance between the corner and the outlet equal to 6δ, and the length upstream of the corner equal to 0.06δ. The number of cells used in the current simulation is 505 in the streamwise and 1000 in the wall-normal directions. In the wall-normal direction, the grid spacing near the wall is $\Delta y^+ = 1.34$ with 10 grid points within $y^+ < 30$.

Validation of the proposed MCT scheme was conducted through comparing the pressure at the wall as well as the velocity profile between the experiments and the simulation. Figure 7 plots the normalized wall pressure of the experimental results versus the RANS results of Oliver [56] and Asmelash [5], and the proposed MCT numerical solver results.

The figure shows that the MCT solution comes closer to predicting the experimental wall pressure than the turbulent RANS models, especially near the ramp edge where MCT captured the first four points of the experimental data while RANS only captured the first point. The difference between the RANS and MCT wall pressure results can be attributed to the convective scheme implemented in each case. In the RANS simulations of the compression ramp, Oliver [56] implemented a first order upwind scheme, and Asmelash [5] implemented a a second order upwind scheme. Here, the MCT scheme is a second-order generalization of the Lax-Friedrichs scheme. It is also worthwhile to mention that the mesh requirement for the MCT case is less demanding compared with a similar DNS study for a compression ramp [87].

The grid spacing near the wall for the MCT case is $\Delta y^+ = 1.34$ with 10 grid points for $y^+ < 30$, while for a similar DNS simulation [87], the required spacing normal to the wall is $\Delta y^+ = 0.2$ with more than 20 grid points in $y^+ < 20$. Unlike the classical DNS relying on fine meshes to resolve subscale motions, MCT formulates subscale motions into the governing equations. Therefore, the mesh requirements for MCT are less restrictive than DNS, resulting MCT as a more computation-friendly theory for turbulent flows. Figure 8 shows the normalized flow velocities at three locations 3δ, 4.2δ, and 5.4δ downstream from the ramp corner, and the MCT numerical solver results. The figure shows that MCT is capable of capturing the boundary layer profile inside the shock.

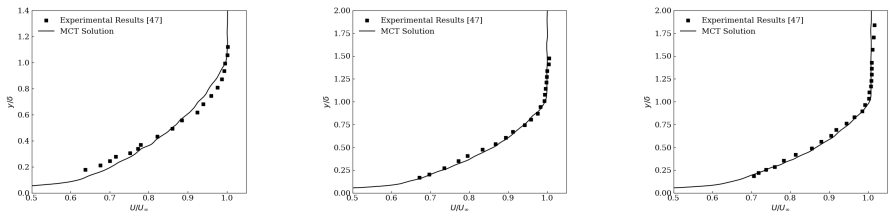

(a) 3δ (b) 4.2δ (c) 5.4δ

Figure 8: Velocity profiles at various locations in the downstream of the ramp edge from the MCT solution and the experiments

As stated previously, the aim of this paper is to investigate the energy transfer between the subscale eddies and the bulk flow inside the shock. Chen stated that the total energy density of each subscale eddy can be expressed as, $E = \frac{1}{2}\left(u_i u_i + j\omega_i\omega_i\right) + e$; where $\frac{1}{2}u_i u_i$ contributes to the translational kinetic energy, $\frac{1}{2}j\omega_i\omega_i$ contributes to the rotational kinetic, and $e = c_v T$ represents the internal energy density of the flow. Analysis of the energy cascade is acheived by the use of the conventional Reynolds averaging (also known as time averaging) method and the mass-weighted averaging method or better known as Favre averaging. The main advantage of these methods is in their ability to resolve the relevant physical processes at different scales [33]. The following notations are used for the mean values: $\langle\ \rangle$ for the Reynolds average and $\{\ \}$ for the Favre average

The scale decomposition employed in the total energy density equation is carried out using Favre filtering in order to account for the density fluctuations of the flow. The Favre decomposition of the total energy density is, $E = \frac{1}{2}\{u_i\}\{u_i\} + \{u_i\}u_i'' + \frac{1}{2}u_i''u_i'' + \frac{j}{2}\{\omega_i\}\{\omega_i\} + j\{\omega_i\}\omega_i'' + \frac{j}{2}\omega_i''\omega_i'' + \{e\} + e''$ The first term on the right hand side $\frac{1}{2}\{u_i\}\{u_i\}$ represents the Favre-averaged mean flow translational kinetic energy, and represents the mean translational speed of the flow. The second term satisfies the relation $\langle\rho\{u_i\}u_i''\rangle = 0$ and may be called the Favre-fluctuating mean flow translational kinetic energy. Huang [40] gives a physical interpretation to the second term by examining the turbulent diffusion in the total energy equation. The final term corresponding to the translational motion is $\frac{1}{2}u_i''u_i''$, and refers to the Favre-fluctuating translational kinetic energy. Similarly, one may define the rotational components of the kinetic energy, the Favre-averaged mean flow rotational kinetic energy as $\frac{j}{2}\{\omega_i\}\{\omega_i\}$, the Favre-fluctuating mean flow rotational kinetic energy as $j\{\omega_i\}\omega_i''$, and the Favre-fluctuating rotational kinetic energy as $\frac{j}{2}\omega_i''\omega_i''$. Finally, $\{e\}$ is the Favre-averaged internal energy, and e'' is the Favre-fluctuating internal energy.

Applying Reynolds averaging over the Favre-decomposed total energy density yields the mean component of the total energy density,

$$\begin{aligned}\langle E\rangle = \{u_i\}\left(\langle u_i\rangle - \frac{\{u_i\}}{2}\right) + j\{\omega_i\}\left(\langle\omega_i\rangle - \frac{\{\omega_i\}}{2}\right)\\ + \frac{1}{2}\langle u_i''u_i''\rangle + \frac{j}{2}\langle\omega_i''\omega_i''\rangle + \{e\} + \langle e''\rangle\end{aligned} \tag{139}$$

The first two terms on the right hand side represent the contribution of the mean translational and mean rotational kinetic energies to the mean total energy density. The next two terms represent the contribution of the averaged Favre-fluctuations to the mean total energy. The $\frac{1}{2}\langle u_i''u_i''\rangle$ term is found in most classical papers discussing turbulence, and is used in the computation of the turbulent Mach number. The other term $\frac{j}{2}\langle\omega_i''\omega_i''\rangle$ is strictly unique to an MCT flow, and represents the fluctuations in the subscale eddies' rotational speed. Therefore, an MCT flow adds to the classical turbulent Mach number a component from the eddies' rotation, $M_t = \frac{\sqrt{\frac{1}{2}\langle u_i''u_i''\rangle + \frac{j}{2}\langle\omega_i''\omega_i''\rangle}}{\langle c\rangle}$ where $\langle c\rangle$ represents the Reynolds average speed of sound.

The last two terms in Eq. 139 represent the contribution of the mean Favre internal energy, and the average Favre-fluctuating internal energy to the mean total energy density. Note that $\{e\} + \langle e''\rangle = \langle e\rangle$. The reason the mean Reynolds

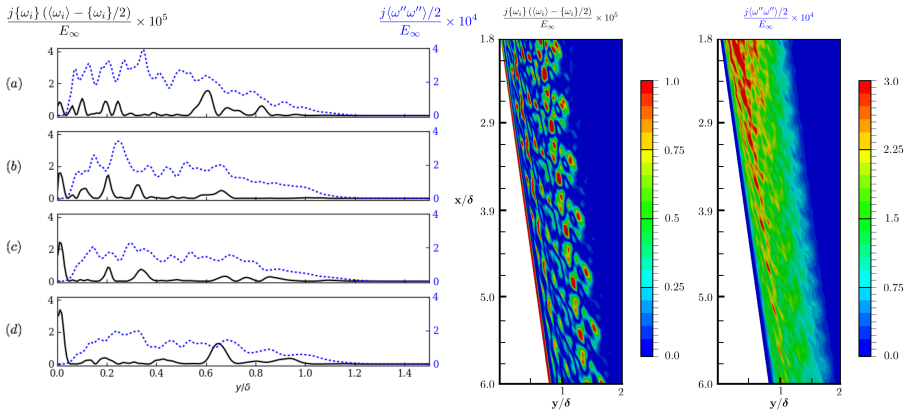

Figure 9: Rotational kinetic energy component of the mean total energy density, mean and fluctuations at (a) 1.8δ, (b) 3δ, (c) 4.2δ, and (d) 5.4δ along the ramp

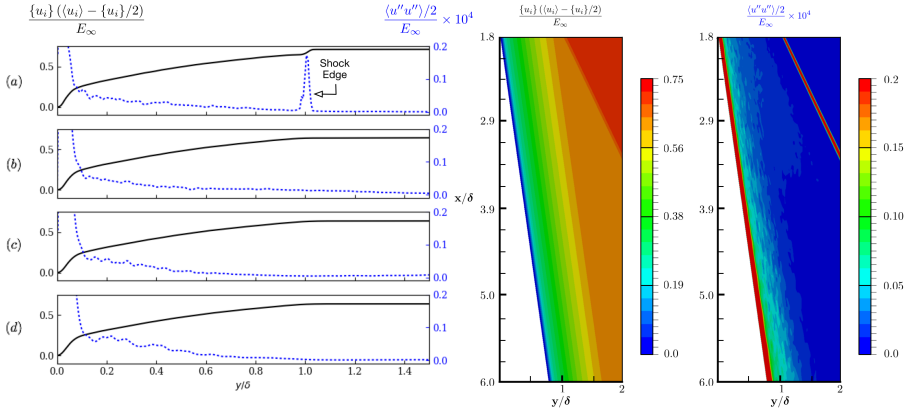

Figure 10: Translation kinetic energy component of the mean total energy density, mean and fluctuations at (a) 1.8δ, (b) 3δ, (c) 4.2δ, and (d) 5.4δ along the ramp

internal energy is not represented is to see the contribution of the Favre fluctuations to the flow.

In order to understand the energy cascade at the level of the subscale eddies, the rotational component of the mean total energy density is investigated. Figure 9 compares the mean rotational component $j\{\omega_i\}\left(\langle\omega_i\rangle - \frac{\{\omega_i\}}{2}\right)$ with the averaged Favre-fluctuating rotational component $\frac{j}{2}\langle\omega_i''\omega_i''\rangle$ at different locations along the ramp. The variables were normalized with respect to the the freestream total energy density $E_\infty = \frac{1}{2}U_\infty^2 + c_v T_\infty$. The figure clearly shows that the averaged component of the rotational kinetic energy density is zero outside the boundary layer indicating an irrotational bulk flow, as was specified at the inlet boundary ($\langle\omega_i\rangle_{inlet} = 0$). Near the wall ($y/\delta < 0.1$), an increase in the magnitude of the averaged component of the rotational kinetic energy density is clearly observed, which can be attributed to the shear forces arising from the wall as well as the diffusion of the near-wall eddies as is clear in the contour plot

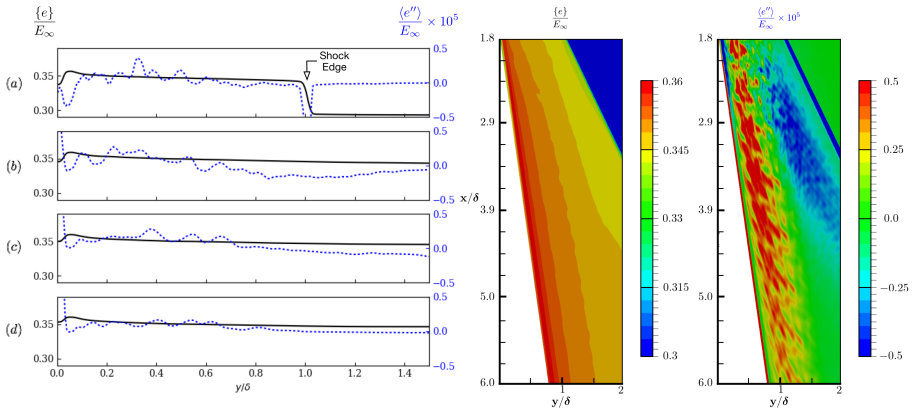

Figure 11: Internal energy component of the mean total energy, mean and fluctuations at (a) 1.8δ, (b) 3δ, (c) 4.2δ, and (d) 5.4δ along the ramp

of Figure 9. Inside the boundary layer but away from the wall ($0.1 < y/\delta < 1$), the figure shows areas with large values of mean rotational kinetic energy, indicating the presence of eddies. It can be seen from the figure that the eddies near the boundary layer are more are tightly packed then the eddies near the walls which are more stretched and elongated. The fluctuating component of the rotational kinetic energy starts out with a large magnitude and decays as it moves along the ramp to less than a half. The reason for having large values of the fluctuation near the ramp edge is due to their proximity to the inlet, which has a boundary condition to generate turbulence by adding fluctuations to the rotational speed of the flow ($\langle \omega_i' \omega_i' \rangle_{inlet} = \omega_{rms}^2$). Moreover, the profile of the fluctuations at $x/\delta = 1.8$ is consistent with the inlet condition, since the turbulent rotational speed is defined inside the boundary layer and diminishes at the edge of the boundary layer. Finally, when comparing the fluctuations along the ramp, the plot shows a large number of local minima and maxima near the ramp edge, with rapid variation between each extremum. This trend implies that there are a lot of small subscale eddies, each separate from the other, as is clear in the contour plot of $\frac{j}{2}\langle \omega_i'' \omega_i'' \rangle$. Further along the ramp, the plot for $\frac{j}{2}\langle \omega_i'' \omega_i'' \rangle$ shows fewer local minima and maxima with a slower rate of change for each extremum. The results imply that a lot of the previous small subscale eddies merge together or diffuse into the mean flow. This behavior is evident from the contour of $\frac{j}{2}\langle \omega_i'' \omega_i'' \rangle$. The impact of rotational kinetic energy on the translational kinetic energy and internal energy will be shown in the following discussions.

Starting with the translational kinetic energy, figure 10 plots the normalized mean components of the translational kinetic energy $\{u_i\}\left(\langle u_i \rangle - \frac{\{u_i\}}{2}\right)$ as well as the normalized averaged Favre-fluctuating components $\frac{1}{2}\langle u_i'' u_i'' \rangle$ at different locations along the ramp. It can be seen from the figure that the biggest contributor to the total energy is the mean translational kinetic energy component of the flow, with the averaged Favre-fluctuations component being smaller than the freestream total energy by four orders of magnitude. The behavior of the averaged Favre-fluctuations translational kinetic energy is decomposed into the

near-wall section ($y/\delta < 0.1$), and the boundary layer section ($0.1 < y/\delta < 1$). For the near-wall part, an increase in the magnitude is observed along the streamwise direction. This increase is highly associated with the shear forces arising from the wall, as well as the increase in the rotational speed of the subscale eddies near the wall. The boundary layer section shows an increase in the average Favre-fluctuating translational kinetic energy along the ramp, coinciding with the decrease of the average Favre-fluctuating rotational component of the flow. In summary, the eddies' rotational energy is dissipated into the translational fluctuating energy.

The other aspect of this energy transfer involves the transmission of rotational kinetic energy to internal energy. Figure 11 compares the Favre-averaged internal energy $\{e\}$ with the averaged Favre-fluctuating internal energy $\langle e'' \rangle$ at different locations along the ramp. From the figure, it is evident that the mean component of the internal energy is constant except near the wall where it is increasing in magnitude along the streamwise direction. The averaged Favre-fluctuating internal energy, away from the wall starts with a maximum value of 0.4 and decreases along the streamwise direction. The large value near the ramp edge, and the large oscillations in the averaged Favre-fluctuating internal energy is directly related to the rotational speed of the subscale eddies, and in particular the averged Favre-fluctuating rotational component of the total energy density. When the averged Favre-fluctuating rotational kinetic energy component of the total energy is high, this increase in turn leads to high fluctutations in the averaged Favre-fluctuating internal energy $\langle e'' \rangle$, as the averged Favre-fluctuating rotational kinetic energy decays along the ramp so does the averaged Favre-fluctuating internal energy. One can conclude that the fluctuations in the internal energy are created from the fluctuations in rotational kinetic energy. Still as the eddies move along the streamwise direction, they diffuse and merge with the mean component of the energy, resulting in a decay in the average fluctuating component of the internal energy. Figure 11 clearly confirms that along the streamwise direction a decay in the fluctuating component of the internal energy occurs.

3.3 Validation 2: Transonic Turbulence over an Asysmetric Hill

An inlet boundary layer profile with a thickness of $\delta = 0.039m$ was specified with an otherwise uniform flow of $M_\infty = 0.6$ at the inlet of a $20H \times 3.205H \times 10H$ domain with $H = 0.078m$ as per Castagna et. al. [11]. The inflow velocity profile was specified by using the mean velocity of the precursor simulation done by Castagna et. al. [11] and comparing the profile with the inflow profile measured experimentally by Simpson [67]. Figure 13 shows that the inflow profiles match very well near the wall and overpredict the velocity in the log layer where $y^+ > 60$. The profiles share a boundary layer thickness of $\delta = \frac{H}{2} = 0.039m$. This discrepancy was kept to see if MCT could still capture experimental flow phenomena in the bulk flow. Turbulent fluctuations were specified by equating the root-mean-square (rms) of the new variable of gyration with the root-mean-square (rms) velocities specified by Castagna et. al. and compared with Spalart [11, 69]. Figure 14 compares the normalized root-mean-square data from MCT and Castagna et. al. with the experimental data obtained by Spalart [69]. The discrepancies are the same for both MCT and Castagna et. al. , since the

data by Castagna et. al. was directly transferred to the gyration variable, via the expression $\sqrt{j}\omega_{i,rms} = u_{i,rms}$. Therefore, the kinetic energy generated by fluctuations in the velocity profile by Castagna et. al. matches the rotational kinetic energy produced by the gyration. Discrepancies between the DNS and experimental data were most notable in the log-layer. These discrepancies were preserved in the gyration, again to see if MCT could still produce better agreement with experiment given the same initial flow data. Inflow density, total

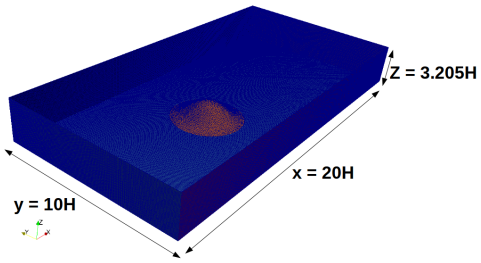

(a) Internal Mesh

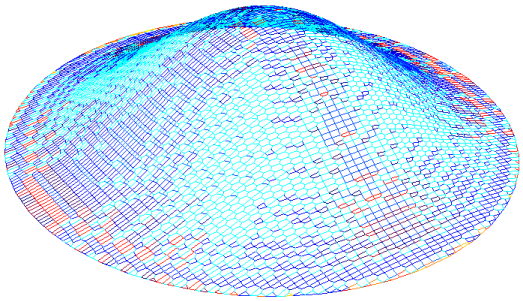

(b) Hill Mesh

Figure 12: Wireframe of the meshes for the rectangular domain and hill. Axisymmetric hill was set at 8.4H away from the interior.

viscosity $\mu + \kappa$, and freestream velocity U_∞, were all set to ensure the Reynolds number, Re_H, based on the height H matched the value of 6500 by Castagna et. al. The time-step for the MCT simulations was 5×10^{-8} s, shorter than the value of 3.04×10^{-5} s by Castagna et. al.. The smaller mesh cells near the wall required these small time step values, but the resulting data benefited from increased temporal accuracy. The wall-normal mesh distribution was set to have a simple grading whereby the last cell away from the wall would be 200 times the length of the smaller cell near the wall. Non-reflective boundary conditions were set at the top and outlet of the domain to prevent unphysical pressure effects from affecting the dynamics at the hill and to follow the setup by Castagna et. al. [11]. Periodic boundary conditions were set in the spanwise direction, also in line with the conditions by Castagna et. al. [11]. Zero gradient, and no-slip boundaries for the velocity, were set at the floor and hill. The mesh near the hill was tailored to the shape of the hill, determined by the mathematical functions set in Castagna et. al. [11]. Table 4 lists the key

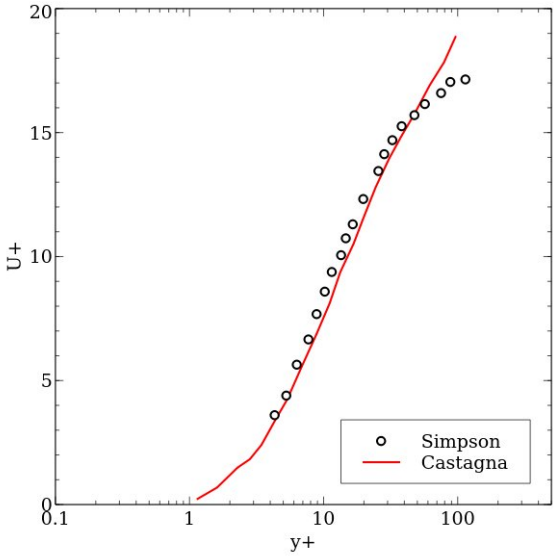

Figure 13: Comparison of DNS inlet profile obtained by Castagna et. al. [11] from a precursour simulation with the experimental profile used by Simpson [67] .

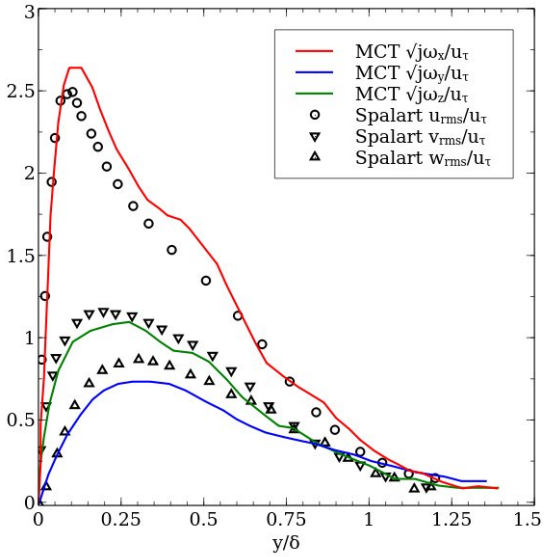

Figure 14: Comparison of MCT/DNS velocity perturbations the DNS profile obtained by Spalart [69].

statistics associated with this custom mesh. A key note is the number of cells for this mesh, totaling around 6.7M elements. With the unstructured mesh, however, the viscous sublayer, defined by the limit $z^+ < 10$, contained 30 cells as opposed to the 10 cells needed in the mesh by Castagna et. al. [11]. Still, the argument that MCT can provide results comparable to DNS data without the

Parameter	Value
Maximum Aspect Ratio	8.62886
Time Step	5×10^{-8} s
Maximum Skewness	5.124
Δz^+_{min}	0.148
Number of cells: $z^+ < 10$	30
Total Number of Cells	6.72×10^6

Table 4: Parameters for mesh quality and time resolution used in MCT simulations

associated computational costs is supported by the dramatic decrease in mesh cell number.

Three non-dimensonal parameters to gauge the onset of turbulence are introduced by Peddieson [59] and are later explained by Wonnell and Chen [85] . These parameters can be extracted from the governing equations through dimensionless analysis [59]. For incompressible flow over a flat plate, these parameters produced turbulent velocity profiles within a boundary layer that matched experimental data produced by the European Research Community on Flow, Turbulence and Combustion (ERCOFTAC) [19]. The parameters are defined as follows:

$$\alpha_1 = \frac{\kappa}{\mu}, \quad \alpha_2 = \frac{\kappa}{\rho\sqrt{j}\,U}, \quad \alpha_3 = \frac{\gamma}{\mu j} \tag{140}$$

In the flat plate study, α_1 proved to be the pivotal parameter in matching an experimental turbulent profile [19]. This parameter serves as a ratio between the particles' contribution to the Cauchy stress, $\kappa\epsilon_{klm}\omega_{m,l}$ and the classical viscous diffusion term, μv_{ll}, in the linear momentum equation. Local variation in the gyration of the particles leads to a tension in the fluid that disrupts the otherwise smooth laminar flow. The classical viscous diffusion attempts to smooth disruptions created by differences in gyration, and so the balance of these forces is critical for determining whether a flow has reached a turbulent state. This result indicates that the tension created by differences in rotational motion of particles needs to exceed viscous diffusion by a considerable amount in order to maintain turbulence within an incompressible boundary layer.

Table 5 gives the values of the three dimensionless parameters for α_n that successfully generated turbulence in the incompressible case. The problem of capturing sub-grid length scales becomes more important when the turbulence becomes more compressible, as the smallest eddies could be impacted by density fluctuations. The balance of compressibility with viscous fluctuations occurs at all scales of motion. This balance is reflected in the new total viscosity, $\mu + \kappa$, of the fluid found in the Reynolds number, Re_H. The contribution of individual structures to the total viscous resistance of the fluid is captured through κ. This simulation incorporates no sub-grid models and will allow for the effects of compressible turbulence to be taken into account. Results were obtained after the freestream flow made 1.2 trips through the domain to follow the example of Castagna et. al., or around $t = 0.009s$ [11].

Figure 15 highlights the formation of the separation bubble on the windward side of the hill using streamlines of the flow along the centerline $y = 0$. The lee-

Parameter	Value
α_1	99
α_2	0.0014
α_3	0.235
$M_\infty = \frac{U_\infty}{c}$	0.6
$Re_H = \frac{\rho_\infty U_\infty H}{\mu + \kappa}$	6500

Table 5: Dimensionless parameters α_n, Mach Number M, and the Reynolds number matching DNS [11, 67, 19]. Speed of sound determined for air at $T_\infty = 293K$

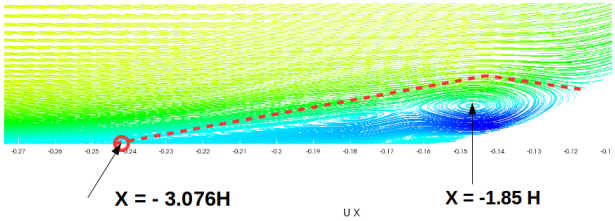

Figure 15: Streamline compared with separation bubble boundaries obtained by Castagna et. al. [11]. MCT data demonstrate a larger windward side separation bubble, but no significant separation on the leeward side. MCT bubble delineated by red dotted line.

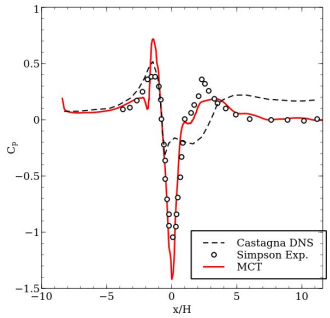

Figure 16: Comparison of $C_p = \frac{p_{static} - p_{atm}}{.5 * \rho * U_\infty^2}$ between experimental data from Simpson, simulation data from Castagna et. al., and numerical data along the centerline $z = 0$ [67, 11].

ward side does not show any apparent separtion bubble. Meanwhile the outline of the MCT windward side bubble falls slightly below some of the recirculation in the MCT data. The reattachment point for the MCT data, at $x = -1.66H$, is slightly downstream than the prediction by Castagna et. al. at $x = -1.7H$, but the size of the windward bubble in MCT clearly exceeds the predictions by Castagna et. al. Inflow turbulence generated near the wall from the gyration and velocity fluctuations may have lead to a much earlier separation point for the MCT flow.

Figure 16 shows that experimental data for the pressure coefficient obtained from Simpson [67] line up more closely with MCT than the numerical results from Castagna et. al. [11]. These successful comparisons add confidence to

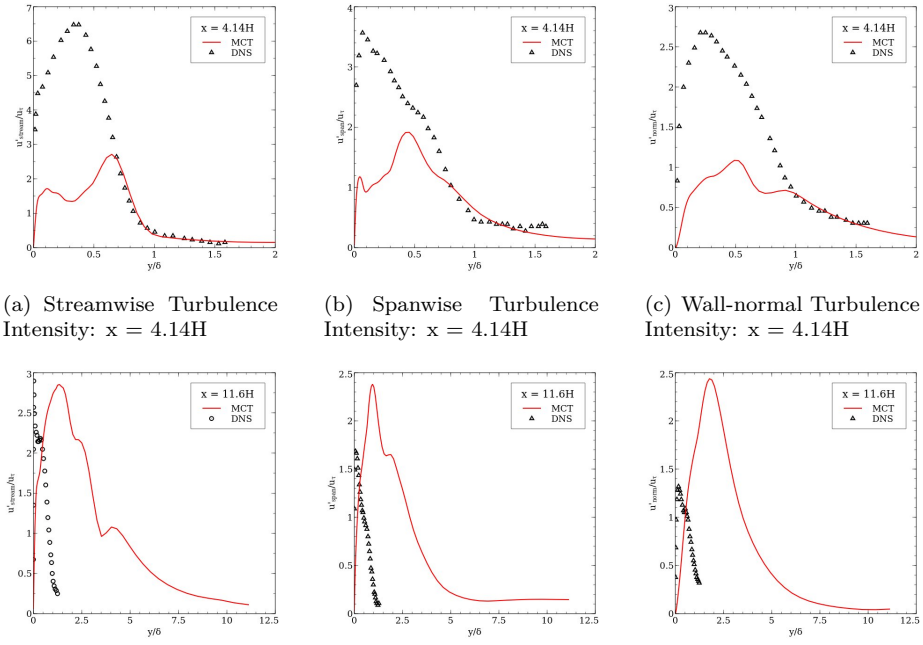

(a) Streamwise Turbulence Intensity: x = 4.14H

(b) Spanwise Turbulence Intensity: x = 4.14H

(c) Wall-normal Turbulence Intensity: x = 4.14H

(d) Streamwise Turbulence Intensity: x = 11.6H

(e) Spanwise Turbulence Intensity: x = 11.6H

(f) Wall-normal Turbulence Intensity: x = 11.6H

Figure 17: Comparison of turbulence intensities, averaged in the spanwise direction, at $x = 4.14H$ and $x = 11.6H$ with DNS data obtained by Castagna et. al. [11].

the statement that numerical simulations of MCT produce realistic, physical flow data without the need for excessively dense grids or high computational costs. The pressure peak downstream of the hill appears at $x = 2.311H$. The DNS study failed to capture this peak, but MCT clearly demonsrates a local peak in this region. After this peak, MCT captures the further evolution of the wall pressure while the data by Castagna et. al. overpredicts the surface pressure. The rapid differences in the vorticity found near the secondary local peak are likely the cause of the local variance in pressure. Simpson noted that the pressure coefficient could be directly related to the vorticity flux [67], and the resolution of this vorticity near the wall likely helps the resolution of the surface pressure.

Near the wall, turbulent fluctuations in MCT data behave in recognizable patterns, but contain noticeable differences from Navier-Stokes simulations. Figure 17 compares the turbulence intensities from Castagna et. al. [11] and MCT data at the same Reynolds number. The MCT turbulence intensities are calculated from gyration. The gyration variable is considered as a stochastic variable and used to perturb the velocity field. The MCT turbulence intensities (I) are obtained by finding the root-mean-square value of gyration

$$\omega_{\text{rms}} = \sqrt{\frac{1}{N}\sum_{k=1}^{N} \omega_i' \omega_i'} \qquad \text{and} \qquad I = \frac{\omega_{\text{rms}}\sqrt{j}}{u_\tau} \tag{141}$$

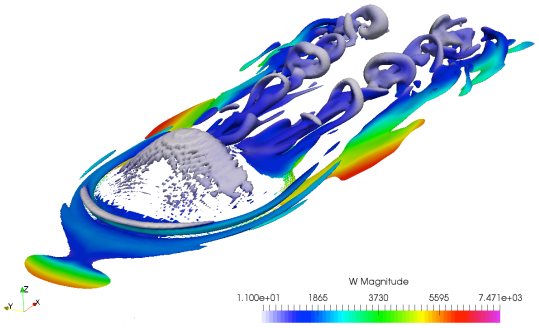

(a) Hairpin Vortices: t = 0.016001 s

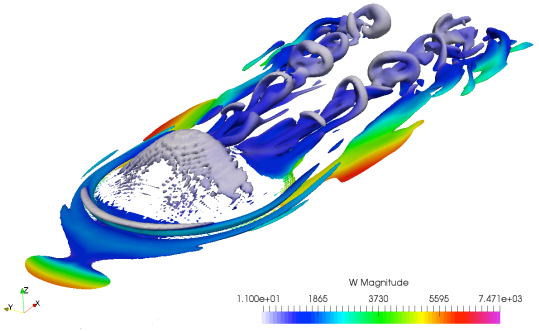

(b) Hairpin Vortices: t = 0.016105 s

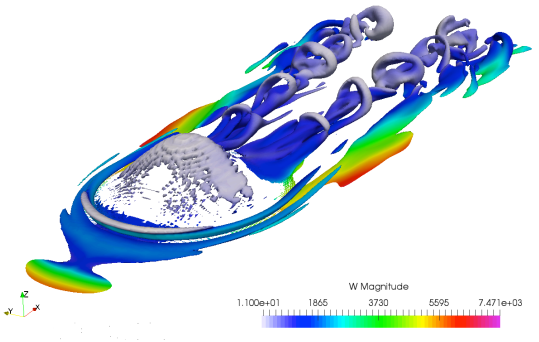

(c) Hairpin Vortices: t = 0.016210 s

Figure 18: Topology of hairpin vortices as visualized by the Q-criterion at 5×10^5, colored by the values of the gyration. Low gyration values for hairpin vortex indicate less variation in small-scale rotation.

Qualitatively similar results are found near the edge of the boundary layer downstream of the hill, and near the wall upstream of the hill. MCT results demonstrate the characteristic peak and decline in turbulence intensity, with

some noticeable differences in the wall-normal data. Downstream of the bump at $x = 11.6H$, the boundary layer in the MCT data shrinks considerably, leading to a wider spread of the turbulence intensity. The downstream behavior is likely affected by the formation of structures such as hairpin vortices.

More in-depth information of the structure of the flow is found using the MCT Q-criterion [15]. Figure 18 shows the isosurface of the Q-criterion colored by the gyration. Figure 18 reveals structures within the turbulence, and particularly hairpin vortices downstream of the hill. Periodic regular hairpin vortices emerge for the Q-value of 5×10^5, with the arches of these vortices characterized by a low value of gyration. Since these structures are all described by the same value for the Q-criterion, these lower regions of gyration must correspond to higher values of velocity gradients. Here, the macroscale component of the flow is dominant. Near the floor, however, gyration plays a more critical role in determining local evolution of structure near the wall. Overall, the new Q-criterion provides the tool to visualize the evolution of large-scale structures that form within the flow and see how small and large scale rotations affect the dynamics and topology of the bulk flow.

3.4 Application: Translational and Rotational Nonequilibrium

The current section employs the first order approximation to the Boltzmann-Curtiss equation to investigate the shock structure in monatomic and diatomic gases. The problem of shock wave structure is selected as it represents a flow regime which is far from thermodynamic equilibrium. Moreover, this problem deals with a one-dimensional flow, in which the impact of the mean gyration of the flow is null, and the gyration equation behaves as transport equation carrying a flow property that doesn't contribute to the physics of the flow. Also, the complexity of the boundary condition selection and its interference with the solution is eliminated by considering this problem. Therefore, this problem focuses on the effect of the bulk viscosity model for the shock wave profiles.

By employing the previous assumptions, and recovering the definition of η, the stress tensor becomes symmetric, i.e.

$$t_{kl} = -p\delta_{kl} - \frac{\mu}{3} U_m x_m \delta_{kl} + \mu \left(U_l x_k + U_k x_l \right) \tag{142}$$

With the new interpretation of the material parameter η, the MCT heat flux vector becomes

$$q_k = -4\mu \frac{k}{m} T x_k \tag{143}$$

This heat flux exhibits a linear relation with temperature gradient, similar to Fourier's law of thermal conduction, with a thermal conductivity dependent on the product of the temperate and the relaxation time. However, the new expression for the thermal conductivity shows that the specific heat is approximately four times the gas constant if a unity Prandtl number is considered. This ratio agrees with the estimated range reported in the NASA technical report [78] for the calculation of the viscosity and thermal conductivity of gases based

on Lennard-Jones potential, which shows that the ratio for diatomic nitrogen is varying between 3.501 to 4.545 at ranges of temperature from $100 - 5000K$.

With new expressions for the stress tensor and heat flux vector, they can be plugged back into the balance laws described earlier for validation with the DSMC results and experimental measurements and direct comparison with the nonequilibrium solution from NS equations. A power law model of the relaxation time as a function of the temperature is employed. Note that this approximation does not physically contradict with the derivation of the material parameter μ, which is a function of the product of the temperature and the relaxation time. It, instead, ensures a consistent intermolecular interaction model while comparing with DSMC and NS solutions (e.g. [65, 9]).

The specific heats and the internal energy of the molecules are obtained in accordance with the principle of equipartition of energy. Since a single temperature is used in the proposed formulation to describe thermodynamic equilibrium (i.e. both rotational and translational equilibrium), the Landau-Teller-Jeans equation [42] is included in diatomic gas simulations to extract rotational and translational temperatures. The approximate expression for the rotational collision number obtained by Parker [57] is considered for the calculation of the rotational relaxation time constant.

The finite volume solver used in this study employs a forward Euler temporal discretization for the unsteady term. In order to have a nonoscillating solution in a hypersonic flow regime, a second order flux splitting scheme introduced by Kurganov, Noelle and Petrova (KNP) [49] is used in the calculation of the convective term at the interfaces. All diffusion terms are computed using central differencing. The spatial accuracy has proven to be second order by following a rigorous verification and validation procedure proposed by Roy et. al. [62, 63]. The full description of the code, as well as the verification and validation results, were presented and published in the 2019 AIAA SciTech Forum.

3.4.1 Shock Structure for Monatomic Gases: Argon

Numerical simulations of shock wave structure in argon gas are performed at different Mach numbers up to Mach 9 on 3000 uniform cells, which span approximately 40 upstream mean free paths. Any computed flow property Q is normalized in the familiar way

$$Q_{\text{normalized}} = \frac{Q - Q_1}{Q_2 - Q_1} \tag{144}$$

where subscripts 1 and 2 refer to the upstream and downstream of the shock respectively. The axial distance x is normalized by the upstream mean free path λ.

In order to show an overall comparison between the solution obtained from the current study and the experimental measurements as well as other numerical simulations of the shock structure, the reciprocal shock thickness, $\frac{d\rho}{dx/\lambda}$ at $\rho_{\text{normalized}} = 0.5$, is calculated and compiled into one graph for the Mach number range from Mach 1.2 to Mach 9. DSMC and NS data are re-printed from the existing literature [65]. As shown in figure 19, NS simulations predict far too thin shock wave, while the DSMC solution perfectly agrees with the experimental data. The current solution shows significantly improved shock thickness than NS solution. Also, the current solution and Burnett results, obtained by

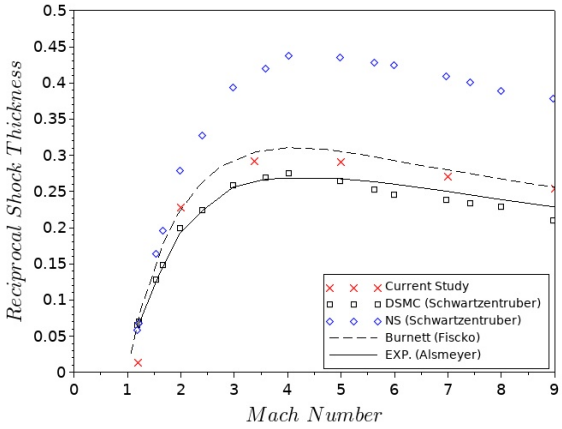

Figure 19: Comparison of argon's reciprocal shock thickness

Fiscko and Chapman [29], are almost identical, and both predict a slightly thinner shock wave than DSMC and experimental results of Alsmeyer [3]. It should be noted that at transonic Mach numbers, i.e. the Mach range from 1 to 1.3, all simulations predict the same shock thickness as the experimental data, since the flow is still at thermal equilibrium. However, as the Mach number increases to supersonic and hypersonic speeds, the shock thickness predicted by NS simulations significantly deviates from DMSC and experimental data. The current study agrees well with the experimental measurements with only less than 10 % difference while the NS simulation results show as much as 60% differences.

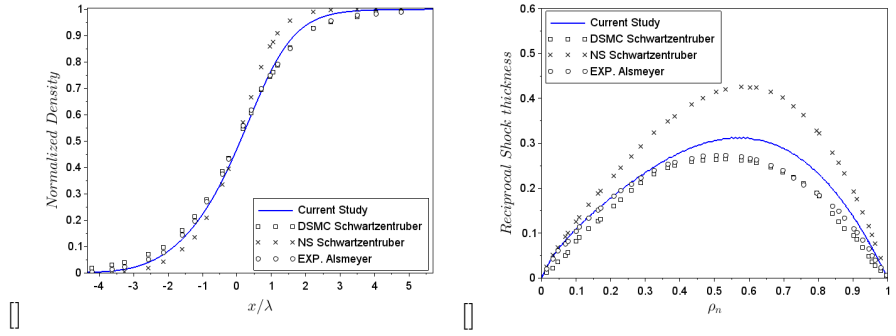

Figure 20: Shock structure of argon at Mach 3.38. (a) Density profile; (b) Reciprocal shock thickness

A more detailed representation of the density profile at Mach 3.38 is shown in figure 20. The reciprocal shock thickness, $\frac{d\rho}{dx/\lambda}$, confirms that the first order solution to the Boltzmann-Curtiss equation predicts a more realistic thicker shock wave and closer to experimental and DSMC predictions than the nonequilibrium NS solution. This improvement can be explained as following: equilibrium in Boltzmann distribution function is restricted to transnational motion only. However, equilibrium in Boltzmann-Curtiss theory requires not only ve-

locity, but both gyration and velocity of molecules dependently to obey the velocity-gyration based Boltzmann-Curtiss distribution. When the gyration is zero, i.e. for moantomic gases, the velocity distribution function recovers to the classical Boltzmann velocity distribution function. The nonequilibrium distribution function, which lead to NS equations, assumes a first order deviation from translational equilibrium only (i.e. equilibrium velocity distribution not velocity-gyration distribution). However, the nonequilibrium distribution function obtained from the first order solution to Boltzmann-Curtiss equation extends nonequilibrium to rotational motion. Since only few collisions are required for translational equilibrium, the time required to recover rotational equilibrium is greater than that for translational equilibrium. Hence, the relaxation time employed in the first order approximation to Boltzmann-Curtiss equation in the current study is larger when compared to the relaxation time in the first order approximation to Boltzmann equation that lead to NS equations. Therefore, the nonequilibrium distribution function obtained in the current study represents further departure from translational equilibrium than the classical Maxwellian nonequilibrium distribution function for monatomic gases. In other words, the bulk viscosity of the stress tensor derived from the Boltzmann-Curtiss distribution is accounting for this deviation.

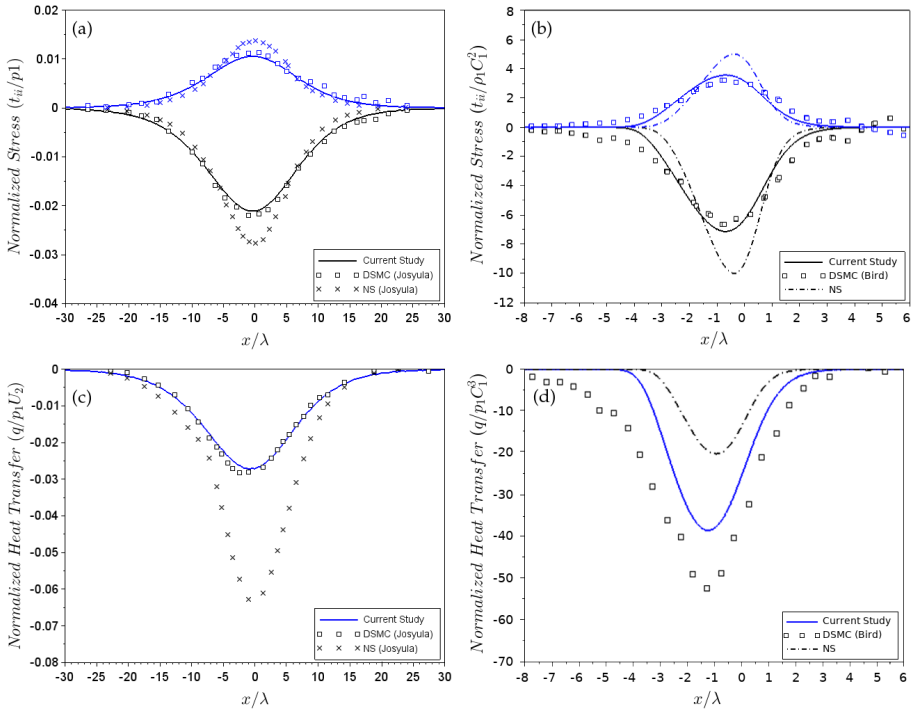

Figure 21: Argon normal stresses and heat flux, at Mach 1.2 (a & c) and Mach 8 (b & d). Figures (a) and (b) show the normal stresses with color black for t_{xx}, blue: t_{yy}, and figures (c) and (d) show the heat flux Normal stresses of argon,;

Figure 21(a-b) shows the normal stress distribution obtained from the currents solution, NS solution and DSMC results for Mach 1.2 and 8. In order to obtain a comparison with DSMC results at a wide Mach number range, the

DSMC data are printed from different sources [44, 8]. The stresses in x and y directions are normalized in a similar way as described in [44, 8], where 1, ρ_1 and C_1 are the upstream pressure, density and most probable molecular velocity respectively. The corresponding heat flux is shown in figure 21(c-d).

At Mach 1.2, NS solution predicts slightly higher peak stresses and much higher heat flux than DSMC solution, while the current solution exactly matches DSMS results. At Mach 8, NS solution significantly deviates further from DSMC results in both stress and heat flux, while the current solution still shows an overall improvement in the prediction of the normal stresses and heat flux as anticipated.

3.4.2 Shock Structure for Diatomic Gases: Nitrogen

The next set of simulations is carried out for nitrogen, a diatomic gas. Solutions are generated at Mach numbers of 1.2, 5 and 10 for upstream conditions of $\rho_1 = 1.225\ kg/m^3$ and $T_1 = 300\ K$. The overall reciprocal shock thicknesses is compared to experimental data of Alsmeyer [3], Camac [10], NS and DSMC results [9] as shown in figure 22. Similar to the argon case, the current solution successfully predicts a wider shock and a more accurate density profiles than NS solution at hypersonic conditions where both translational and rotational nonequilibrium exist. Also, the current study is shown to agree well with the DSMC solution.

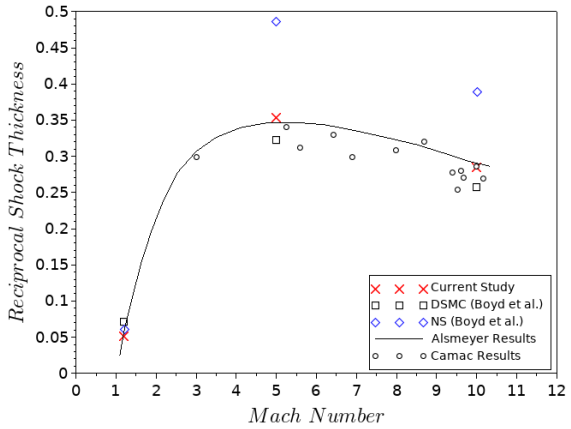

Figure 22: Comparison of nitrogen's reciprocal shock thickness

More detailed comparisons of the density and temperature profiles are shown in figure 23(a-f) for Mach numbers 1.2, 5 and 10. At Mach 1.2, the density and temperature profiles of the three solutions are almost identical with a slight difference between the translational (black) and rotational (blue) temperatures. As the Mach number increases, NS density and temperature profiles deviate further from DSMC results. Note that DSMC results are taken as a reference as it best matches experimental measurements of density profiles. Also, it is useful for comparing temperature profiles as no experimental data exist in the literature on the temperature profiles inside the shock-wave. Overall, the density

profiles obtained from the current solution matches the DSMC predicted profile with noticeable discrepancy for the temperature profile. However, since there is a lack of experimental measurements of temperature inside the shock wave, this discrepancy in the temperature profiles requires further investigations. It should also be noted that DSMC is a solution to Boltzmann equation not to Boltzmann-Curtiss equation.

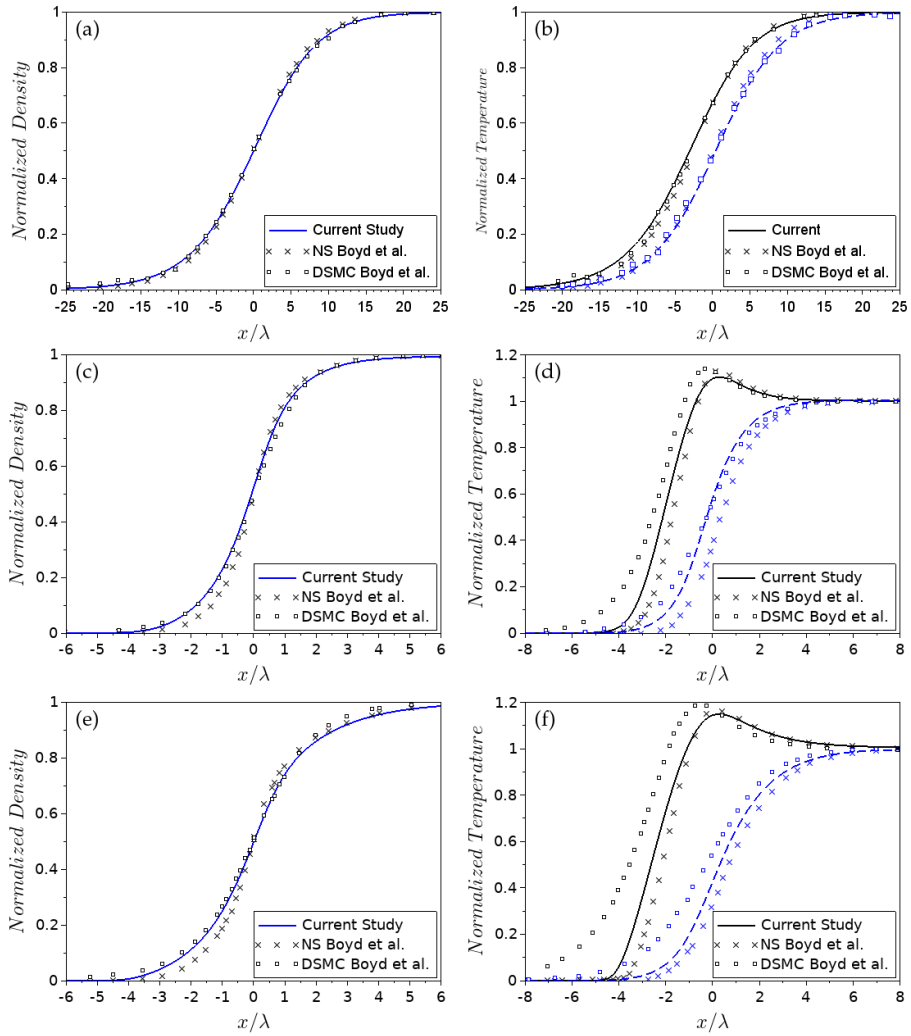

Figure 23: Nitrogen density and temperature profile (black: translation, blue: rotation) at Mach 1.2 (a & b), Mach 5 (c & d), and Mach 10 (e & f).

4 Personnel & Recognition

This project has been supporting the PI and four gradate students. Up to date, the PI has graduated two doctoral student and one master students expected

to graduate this summer under the support of this award. The team has been recognized in numerous occasions.

1. James Chen (PI)
    - Promoted to Associate Professor with tenure, 2020
    - Exceptional Scholar – Young Investigator Award, University at Buffalo - State University of New York, 2019
    - Outstanding Young Engineer Award, Wichita Council of Engineering Societies (nominated by AIAA), 2018
    - Steve Hsu Keystone Research Scholar (Endowed Scholarship), 2017-2018
    - Elected as an Honorary Fellow at The Australian Institute of High Energetic Materials, 2017
2. Louis B. Wonnell (PhD) – 2015-2018
    - graduated in Spring 2018 from Kansas State University
    - currently a Postdoctoral Researcher at Oak Ridge National Lab
3. Mohamad Ibrahim Cheikh (PhD) – 2016-2020
    - graduated in Fall 2019 from University at Buffalo
    - APS DFD Travel Award, 2017
    - Graduate Teaching Assistant of the Year, 2017
    - currently a Postdoctoral Researcher at University of Houston
4. Mohamed M Ahmed (PhD student at K-State) – 2017-2018
5. Jiamiao Sun (MS student at UB) – 2019-2020
    - expected to graduate in Spring 2020

5 Publications

Up to date, this project has resulted in two PhD dissertation, nine peer-reviewed journal articles, five peer-reviewed proceeding articles, eleven conference presentations and seven invited talks.

- PhD Dissertation
    1. L. B. Wonnell, "A kinetic analysis of morphing continuum theory for fluid flows," PhD Dissertation, May 2018, Kansas State University
    2. M. I. Cheikh, "A Morphing Continuum Theory for Fluid Flow," PhD Dissertation, Feb 2020, University at Buffalo
- Journal Articles
    1. M. M. Ahmed, M. I. Cheikh and J. Chen, "Boltzmann-Curtiss Description for Flows under Translational and Rotational Nonequilibrium," *Journal of Fludis Engineering,* 142, 051302, 2020

2. M. I. Cheikh, J. Chen and M. Wei, "Small-scale Energy Cascade in Homogeneous Isotropic Turbulence," *Physical Review Fluids*, 4, 104610, 2019
3. T. Yang, M. Wei and J. Chen, "A Monolithic Immersed Boundary Approach to Study Fluid-Solid Interaction of Flexible Wings," *International Journal of Micro Air Vehicle*, 11, 1–13, 2019
4. L. B. Wonnell and J. Chen, "First-order approximation to the Boltzmann-Curtiss Equation for Flows with Local Spins," *Journal of Engineering Mathematics*, 114, 43–64, 2019
5. L. B. Wonnell, M. I. Cheikh and J. Chen, "A Morphing Continuum Simulation of Transonic Flow over an Asymmetric Hill," *AIAA Journal*, 56, 4321–4330, 2018
6. M. I. Cheikh, L. B. Wonnell and J. Chen, "A Morphing Continuum Analysis in Compressible Turbulence," *Physical Review Fluids*, 3, 024604, 2018
7. J. Chen, "Morphing Continuum Theory for Turbulence: Theory, Computation and Visualization," *Physical Review E*, 96, 043108, 2017
8. J. Chen, "An Advanced Kinetic Theory for Morphing Continuum with Inner Structures," *Reports on Mathematical Physics*, 80, 317-332, 2017
9. L. B. Wonnell and J. Chen, "Morphing Continuum Description for Boundary Layer Transition and Turbulence," *Journal of Fluids Engineering*, 139, 011205, 2017

- Proceeding Articles

1. M. I. Cheikh and J. Chen, "Particle-Turbulence Interaction in Homogeneous Isotropic Turbulence," AIAA-2019-3715
2. M. M. Ahmed and J. Chen, "Verification and Validation of a Morphing Continuum Approach to Hypersonic Flow Simulations," AIAA-2019-0891
3. M. I. Cheikh, E. A. Schinstock, G. P. Ferland and J. Chen,"A Molecular Dynamics-Based Model for Knudsen Number and Slip Velocity," Proceeding of the ASME 2017 Fluids Engineering Division Summer Meeting, FEDSM2017-69136
4. L. Wonnell and J. Chen, "Extension of Morphing Continuum Theory to Numerical Simulations of Transonic Flow Over a Bump," AIAA-2017-3461
5. M. I. Cheikh and J. Chen, "A Morphing Continuum Approach to Supersonic Flow over a Compression Ramp," AIAA-2017-3460

- Conference Presentation

1. M. I. Cheikh and J. Chen, "Particle-Turbulence Interaction in Homogeneous Isotropic Turbulence," AIAA Aviation 2019 Forum, Dallas, TX, June 17-21, 2019

2. M. I. Cheikh and J. Chen, "Multiscale Energy Transfer Within Turbulence," Modeling and Simulation of Turbulent Mixing and Reaction: For Power, Energy and Flight, Amherst, NY, April 12-13, 2019
3. M. M. Ahmed and J. Chen, "Verification and Validation of a Morphing Continuum Approach to Hypersonic Flow Simulations," AIAA Scitech 2019 Forum, San Diego, CA, January 7-11, 2019
4. J. Chen and M. M. Ahmed,"An Advanced Kinetic Description for Shock Structure under Hypersonic Conditions," 71st APS DFD Meeting, Atlanta, GA, November 18-20, 2018
5. M. I. Cheikh and J. Chen,"Energy Flows of Homogeneous Isotropic Turbulence at Sub-scale Eddies," 71st APS DFD Meeting, Atlanta, GA, November 18-20, 2018
6. A. Hajesfandiari, H. Zhang and J. Chen,"Boundary Effects in Microchannel Flows," 71st APS DFD Meeting, Atlanta, GA, November 18-20, 2018
7. L. B. Wonnell, M. I. Cheikh, and J. Chen, "Morphing Continuum Theory: A First Order Approximation to the Balance Laws," 70th APS DFD Meeting, Denver, CO, November 19-21, 2017
8. M. I. Cheikh, L. B. Wonnell, and J. Chen, "Energy Cascade Analysis: From Subscale Eddies tp Mean Flow," 70th APS DFD Meeting, Denver, CO, November 19-21, 2017
9. M. I. Cheikh, E. A. Schinstock, G. P. Ferland and J. Chen, "A Molecular Dynamics-Based Model for Knudsen Number and Slip Velocity," the ASME 2017 Fluids Engineering Division Summer Meeting, Waikoloa, HI, July 30 - August 3, 2017
10. L. B. Wonnell and James Chen, "Extension of Morphing Continuum Theory to Numerical Simulations of Transonic Flow over a Bump," 47th AIAA Fluid Dynamics Conference, Denver, CO, June 5-9, 2017
11. M. I. Cheikh and J. Chen, "A Morphing Continuum Approach to Supersonic Flow over a Compression Ramp," 47th AIAA Fluid Dynamics Conference, Denver, CO, June 5-9, 2017

- Invited Talk

1. "Multiscale Energy Transfer within Turbulence," The Burgers Program for Fluid Dynamics (Fluid Dynamics Review Seminar Series) at University of Maryland, September 13, 2019
2. "Multiscale Energy Transfer within Turbulence," Department of Mechanical, Aerospace and Nuclear Engineering at Rensselaer Polytechnic Institute, March 20, 2019
3. "A Kinetic Description for Morphing Continuum," Department of Mathematics at University at Buffalo, October 16, 2018
4. "A Kinetic Description of Morphing Continuum: the zero-th and first order approximation," The Institute for Computational Engineering and Sciences at The University of Texas at Austin, March 29, 2018

5. "A Kinetic Description of Morphing Continuum and Its Applications in Fluid Mechanics," Department of Mechanical and Aerospace Engineering at University of Buffalo, February 19, 2018
6. "A Kinetic Description of Morphing Continuum and Its Applications in Fluid Mechanics," Department of Mechanical and Aerospace Engineering at Case Western Reserve University, January 29, 2018
7. "Research at Multiscale Computational Physics Lab - Advanced Kinetic Theory and Atomistic Electrodynamics," Department of Mathematics at Kansas State University, April 17, 2017

- Media Coverage

1. Aerospace Testing International, Link Here & In Print (July 2019 Issue)
2. Design News, Link Here, April 16, 2019
3. Design Engineering, Link Here, March 20, 2019
4. Futurity, Link Here, March 18, 2019
5. EPeak World News, Link Here, March 15, 2019
6. Space Daily, Link Here, March 14, 2019
7. Electronic Component News, Link Here, March 14, 2019
8. Science Daily, Link Here, March 12, 2019
9. Before It's News, Link Here, March 12, 2019
10. Environmental News Network, Link Here, March 12, 2019
11. Bioengineering.Org, Link Here, March 12, 2019
12. Super Computing Online, Link Here, March 12, 2019
13. Scienmag, Link Here, March 12, 2019
14. NewsWise, Link Here, March 12, 2019
15. TechXplore, Link Here, March 12, 2019
16. EurekAlert, Link Here, March 12, 2019

Acknowledgement/Disclaimer

This task is supported by AFOSR/RTA (Grant number FA9550-17-1-0154, Monitor: Dr. I. Leyva).

References

[1] Ahmadi, G. Turbulent shear flow of micropolar fluids. *International Journal of Engineering Science 13*, 11 (1975), 959–964.

[2] Ahmed, M. M., and Chen, J. Verification and validation of a morph-ing continuum approach to hypersonic flow simulations. In *AIAA Scitech 2019 Forum* (2019), pp. AIAA 2019–0891.

[3] Alsmeyer, H. Density profiles in argon and nitrogen shock waves measured by the absorption of an electron beam. *Journal of Fluid Mechanics 74*, 3 (1976), 497–513.

[4] Ariman, T., and Cakmak, A. S. Couple stresses in fluids. *Physics of Fluids 10* (1967), 24975.

[5] Asmelash, H. A., Martis, R. R., and Singh, A. Numerical simulation of ramp induced shock wave/boundary-layer interaction in turbulent flow. *The Aeronautical Journal 117* (2013), 629–638.

[6] Baraff, D. An introduction to physically based modeling: rigid body simulation i - unconstrained rigid body dynamics. *SIGGRAPH Course Notes* (1997).

[7] Bhatnagar, P. L., Gross, E. P., and Krook, M. A model for collision processes in gases. i. small amplitude processes in charged and neutral one-component systems. *Physical Review 94* (1954), 511.

[8] Bird, G. A. Aspects of the structure of strong shock waves. *The Physics of Fluids 13*, 5 (1970), 1172–1177.

[9] Boyd, I. D., Chen, G., and Candler, G. V. Predicting failure of the continuum fluid equations in transitional hypersonic flows. *Physics of Fluids 7*, 1 (1995), 210–219.

[10] Camac, M. Argon and nitrogen shock thicknesses. In *Aerospace Sciences Meeting* (1964), p. 35.

[11] Castagna, J., Yao, Y., and Yao, J. Direct numerical simulation of a turbulent flow over an axisymmetric hill. *Computers & Fluids 95* (2014), 116–126.

[12] Cheikh, M. I., Wonnell, L. B., and Chen, J. Morphing continuum analysis of energy transfer in compressible turbulence. *Physical Review Fluids 3*, 2 (2018), 024604.

[13] Chen, H., Kandasamy, S., Orszag, S., Shock, R., Succi, S., and Yakhot, V. Extended Boltzmann kinetic equation for turbulent flows. *Science 301*, 5633 (2003), 633–636.

[14] Chen, J. An advanced kinetic theory for morphing continuum with inner structures. *Reports on Mathematical Physics 80*, 3 (2017), 317 – 332.

[15] Chen, J. Morphing continuum theory for turbulence: Theory, computation, and visualization. *Physical Review E 96* (2017), 043108.

[16] Chen, J., Lee, J. D., and Liang, C. Constitutive equations of micropolar electromagnetic fluids. *Journal of Non-Newtonian Fluid Mechanics 166* (2011), 867–874.

[17] Chen, J., Liang, C., and Lee, J. D. Theory and simulation of micropolar fluid dynamics. *Proceedings of the Institution of Mechanical Engineers, Part N: Journal of Nanoengineering and Nanosystems* (2010), 31–39.

[18] Chen, J., Liang, C., and Lee, J. D. Numerical simulation for unsteady compressible micropolar fluid flow. *Computers & Fluids 66* (2012), 1–9.

[19] Chen, J., and Wonnell, L. A multiscale morphing continuum description for turbulence. In *Bulletin of the American Physical Society* (2015), vol. 60, 68th Annual Meeting of the APS Division of Fluid Dynamics.

[20] Cockburn, B., and Shu, C. W. The runge-kutta discontinuous galerkin method for conservation laws v: multidimensional systems. *Journal of Computational Physics 141* (1998), 199–224.

[21] Colella, P., and Woodward, P. R. The piecewise parabolic method (ppm) for gas-dynamical simulations. *Journal of Computational Physics 54* (1984), 174–201.

[22] Curie, P. *Oeuvres de Pierre Curie: publiées par les soins de la Société de physique*. Gauthier-Villars, 1908.

[23] Curtiss, C. F. The classical boltzmann equation of a gas of diatomic molecules. *Journal of Chemical Physics 75* (1981), 376.

[24] Curtiss, C. F. The classical boltzmann equation of a molecular gas. *Journal of Chemical Physics 97* (1992), 1416.

[25] De Groot, S. R., and Mazur, P. *Non-equilibrium Thermodynamics*. North-Holland, Amsterdam, Netherlands, 1962.

[26] Eringen, A. C. Theory of micropolar fluids. *Journal of Applied Mathematics and Mechanics 16* (1964), 1–18.

[27] Eringen, A. C. *Microcontinuum field theories: I. Foundations and Solids*. Springer, 1999.

[28] Eringen, A. C. *Microcontinuum field theories: II. Fluent media*. Springer, 2001.

[29] Fiscko, K. A., and Chapman, D. R. Comparison of burnett, super-burnett and monte carlo solutions for hypersonic shock structure. In *Progress in Astronautics and Aeronautics* (1989), pp. 374–395.

[30] Fowles, G., and Cassidy, G. *Analytical Mechanics*. Thomson, 2004.

[31] Ganapathisubramani, B., Clemens, N. T., and Dolling, D. S. Effects of upstream boundary layer on the unsteadiness of shock-induced separation. *Journal of Fluid Mechanics 585* (2007), 369–394.

[32] Grad, H. Statistical mechanics, thermodynamics and fluid dynamics of systems with an arbitrary number of integral. *Communications on Pure and Applied Mathematics 5* (1952), 455–494.

[33] Guarini, S. E., Moser, R. D., Shariff, K., and Wray, A. Direct numerical simulation of a supersonic turbulent boundary layer at mach 2.5. *Journal of Fluid Mechanics 414* (2000), 1–33.

[34] Gupta, V. K., Shukla, P., and Torrilhon, M. Higher-order moment theories for dilute granular gases of smooth hard spheres. *Journal of Fluid Mechanics 836* (2018), 451–501.

[35] Haller, G. An objective definition of a vortex. *Journal of Fluid Mechanics 525* (2005), 1–26.

[36] Hansen, J. S., Daivis, P. J., Dyre, J. C., Todd, B. D., and Bruus, H. Generalized extended navier-stokes theory: Correlations in molecular fluids with intrinsic angular momentum. *Journal of Chemical Physics 138* (2013), 034503.

[37] Harten, A., Engquist, B., Osher, S., and Chakravarthy, S. R. Uniformly high order accurate essentially non-oscillatory schemes, iii. In *Upwind and High-Resolution Schemes*. Springer, 1987, pp. 218–290.

[38] Hirschfelder, J. O., Bird, R. B., and Curtiss, C. F. *Molecular theory of gases and liquids*. Wiley, 1964.

[39] Huang, K. *Statistical Mechanics*. John Wiley & Sons, 1987.

[40] Huang, P. G., Coleman, G. N., and Bradshaw, P. Compressible turbulent channel flows: Dns results and modelling. *Journal of Fluid Mechanics 305* (1995), 185–218.

[41] Hynes, J. T., Kapral, R., and Weinberg, M. Molecular rotation and reorientation: Microscopic and hydrodynamic contributions. *Journal of Chemical Physics 69* (1978), 2725–2733.

[42] Jeans, J. H. *The dynamical theory of gases*. University Press, 1921.

[43] Jenkins, J. T., and Richman, M. W. Kinetic theory for plane flows of a dense gas of identical, rough, inelastic, circular disks. *Physics of Fluids 28* (1985), 3485–3494.

[44] Josyula, E., and Wadsworth, D. Internal energy mode relaxation in high speed continuum and rarefied flows. In *42nd AIAA Aerospace Sciences Meeting and Exhibit* (2004), p. 1182.

[45] Kirwan Jr, A. Theory of turbulent eddies. *The Physics of Fluids 10*, 9 (1967), S84–S86.

[46] Kremer, G. M. *An introduction to the Boltzmann equation and transport processes in gases*. Springer Science & Business Media, 2010.

[47] Kuntz, D. W. *An experimental investigation of the shock wave turbulent boundary layer interaction*. PhD thesis, University of Illinois, Illinois, USA, 1985.

[48] Kuntz, D. W., Amatucci, V. A., and Addy, A. L. Turbulent boundary-layer properties downstream of the shock-wave/boundary-layer interaction. *AIAA Journal 25* (1987), 668.

[49] Kurganov, A., Noelle, S., and Petrova, G. Semidiscrete central-upwind schemes for hyperbolic conservation laws and hamilton–jacobi equations. *SIAM Journal on Scientific Computing 23* (2001), 707–740.

[50] Liu, X. D., Osher, S., and Chan, T. Weighted essentially non-oscillatory schemes. *Journal of Computational Physics 115* (1994), 200–212.

[51] Lopez, M., Chen, J., and Palochko, V. A. A multiscale study of the boundary layer development for microfluidic system. *Molecular Simulation 42* (2016), 1370–1378.

[52] Martn, M. P. Direct numerical simulation of hypersonic turbulent boundary layers. part 1. initialization and comparison with experiments. *Journal of Fluid Mechanics 570* (2007), 347–366.

[53] McCormack, P. *Vortex, Molecular Spin andNanovorticity.* Springer, 2012.

[54] Montero, S., and Pérez-Ríos, J. Rotational relaxation in molecular hydrogen and deuterium: Theory versus acoustic experiments. *Journal of Chemical Physics 141* (2014), 114301.

[55] Moukalled, F., Mangani, L., and Darwish, M. *The Finite Volume Method in Computational Fluid Dynamics: An Advanced Introduction with OpenFOAM® and Matlab*, 1 ed. Springer, 2015.

[56] Oliver, A. B., Lillard, R. P., Schwing, A. M., Blaisdell, G. A., and Lyrintzis, A. S. Assessment of turbulent shock-boundary layer interaction computations using the overflow code. *45th AIAA Aerospace Sciences Meeting and Exhibit* (2007), 104.

[57] Parker, J. G. Rotational and vibrational relaxation in diatomic gases. *The Physics of Fluids 2*, 4 (1959), 449–462.

[58] Patankar, S. *Numerical heat transfer and fluid flow*, 1 ed. CRC press, 1980.

[59] Peddieson, J. An application of the micropolar fluid model to the calculation of a turbulent shear flow. *International Journal of Engineering Science 10* (1972), 23–32.

[60] Rahimi, B., and Struchtrup, H. Macroscopic and kinetic modelling of rarefied polyatomic gases. *Journal of Fluid Mechanics 806* (2016), 437–505.

[61] Rist, U., and Fasel, H. Direct numerical simulation of controlled transition in a flat-plate boundary layer. *Journal of Fluid Mechanics 298* (1995), 211–248.

[62] Roy, C. J., McWherter-Payne, M. A., and Oberkampf, W. L. Verification and validation for laminar hypersonic flow elds, part 1: Verification. *AIAA journal 41*, 10 (2003), 1934–1943.

[63] Roy, C. J., Oberkampf, W. L., and McWherter-Payne, M. A. Verification and validation for laminar hypersonic flow elds, part 2: Validation. *AIAA journal 41*, 10 (2003), 1944–1954.

[64] Sampson, B. Smooth hypersonic. *Aerospace Testing International* (2019), 16.

[65] Schwartzentruber, T. E., and Boyd, I. D. A hybrid particle-continuum method applied to shock waves. *Journal of Computational Physics 215*, 2 (2006), 402–416.

[66] Shu, C. W., and Osher, S. Efficient implementation of essentially non-oscillatory shock-capturing schemes. *Journal of Computational Physics 77* (1988), 439–471.

[67] Simpson, R. L., Long, C. H., and Byun, G. Study of vortical separation from an axisymmetric hill. *International Journal of Heat and Fluid Flow 23*, 5 (2002), 582–591.

[68] Souverein, L. J., Bakker, P. G., and Dupont, P. A scaling analysis for turbulent shock-wave/boundary-layer interactions. *Journal of Fluid Mechanics 714* (2013), 505–535.

[69] Spalart, P. R. Direct simulation of a turbulent boundary layer up to $r_\theta = 1410$. *Journal of Fluid Mechanics 187* (1988), 61–98.

[70] Speziale, C. G. Invariance of turbulent closure models. *Physics of Fluids 22* (1979), 1033–1037.

[71] Speziale, C. G. Comments on the "material frame-indifference" controversy. *Physics Review A 36* (1987), 4522–4525.

[72] Speziale, C. G. Turbulence modeling in noninertial frames of refeence. *Theoretical and Computaiotnal Fluid Dynamics 1* (1989), 3–19.

[73] Speziale, C. G. A review of material frame-indifference in mechanics. *Applied Mechanics Reviews 51* (1998), 489–504.

[74] Speziale, C. G., Sarkar, S., and Gatski, T. B. Modelling the pressureâ strain correlation of turbulence: an invariant dynamical systems approach. *Journal of Fluid Mechanics 227* (1991), 245–272.

[75] Stokes, V. Couple stresses in fluids. *Physics of Fluids 9* (1966), 1709.

[76] Stokes, V. K. *Theories of fluids with microstructure: an introduction*. Springer Science & Business Media, 2012.

[77] Struchtrup, H. Macroscopic transport equations for rarefied gas flows. In *Macroscopic Transport Equations for Rarefied Gas Flows*. Springer, 2005, pp. 145–160.

[78] Svehla, R. A. Estimated viscosities and thermal conductivities of gases at high temperatures. *NASA Technical Report, NASA-TR-R-132* (1 1962).

[79] Tillotson, B. J., Loth, E., Dutton, J. C., Mace, J., and Haeffele, B. Experimental study of a mach 3 bump-compression flowfield. *Journal of Propulsion and Power 25* (2009), 545.

[80] Truesdell, C. *Continuum Mechanics I: The Mechanical Functions of Elasticity and Fluid Dynamics*. Science, New York, NY, 1966.

[81] Truesdell, C., and Noll, W. The non-linear field theories of mechanics. In *The non-linear field theories of mechanics*. Springer, 2004.

[82] Truesdell, C., and Rajapogal, K. R. *An Introduction to the Mechanics of Fluids*. Birkhauser, Boston, MA, 1999.

[83] Wang-Chang, C. S., Uhlenbeck, G. E., and De Boer, J. The heat conductivity and viscosity of polyatomic gases. *Studies in Statistical Mechanics 2* (1964), 241.

[84] Wonnell, L. B., Cheikh, M. I., and Chen, J. A morphing continuum simulation of transonic flow over an axisymmetric hill. *AIAA Journal 56* (2018), 4321–4330.

[85] Wonnell, L. B., and Chen, J. A morphing continuum approach to compressible flows: Shock wave-turbulent boundary layer interaction. In *46th AIAA Fluid Dynamics Conference* (2016), pp. AIAA 2016–4279.

[86] Wonnell, L. B., and Chen, J. Morphing continuum theory: Incorporating the physics of microstructures to capture the transition to turbulence within a boundary layer. *Journal of Fluids Engineering 139* (2017), 011205.

[87] Wu, M., and Martin, M. P. Direct numerical simulation of supersonic turbulent boundary layer over a compression ramp. *American Institute of Aeronautics and Astronautics Journal 45* (2007), 879–889.

[88] Xu, S., and Martin, M. P. Assessment of inflow boundary conditions for compressible turbulent boundary layers. *Physics of Fluids 16* (2004), 2623–2639.